UNIVERSITY OF OSLO
Department of Physics

Numerical modeling of coupled diffusion-reaction and deformation processes

Master thesis in Physics of Geological Processes

Håkon Storheim

1st June 2011

Preface

I would like to thank my supervisors, Anders Malthe-Sørenssen and Marcin Dabrowski, for good help and guidance throughout the year. Although the main goal not always was defined, we ended with a good story. Especially thanks to Marcin for sending me to Vienna and EGU, and for all the late evenings with helpfull discussions and programming.

My time at Physics of Geological Processes (PGP) has been super, and I am grateful for all the knowledge and fun I have had here!

Thanks to "the lovely master students", Kristin(x2), Elvira, Øystein, Pål, Lienne, Even and Audun. For great fun and a lot of support. I sure hope we stay in contact after PGP!

My friends and family also deserve thanks for their support and encouragement.

Many thanks to my fantastic girlfriend Anna!

Oslo, June 1, 2011

Håkon Storheim

Contents

Chapter 1

Introduction

In the recent years there has been a focus on the CO_2-increase in the atmosphere and what consequences this has for the climate. The anthropogenic release of CO_2 has increased dramatically since the pre-industrial time, and there has been proposed several methods for storage of CO_2. In the IPPC Special report on Carbon Dioxide Capture and Storage (IPCC (2005)) different methods are suggested such as, injection of CO_2 into depleted oil and gas reservoirs, disposal of CO_2 in deep saline aquifers or in the deep sea. An alternative to these methods is in-situ mineralogical storage, which is still on the research stage, but is likely the most permanent way of CO_2 storage. Mineral carbonation means fixation of CO_2 as stable carbonates such as calcite, dolomite or magnesite (Lackner et al. (1995), Giammar et al. (2005), Oelkers et al. (2008)). At Earth's surface conditions carbonates are energetically favoured to form from the interaction of CO_2 with silicates. Mg-silicates such as forsteritic olivine (Mg_2SiO_4), may react with CO_2 to form magnesite according to the following reaction:

$$Mg_2SiO_4 + 2CO_2 \rightarrow 2MgCO_3 + SiO_2$$

Peridotites (olivine rich rocks) are found to react extensively with CO_2-bearing fluids, eventually resulting in the formation of ophicarbonates (Bucher and Frey (2002)). Tectonics and surface erosion have resulted in surface exposure of numerous outcrops of mantle peridotite, for example in the Røragen-Feragen complex in Norway (Moore and Hultin (1980)), in the ultramafic bodies of the alps (e.g. Trommsdorff et al. (1980), Fruh-green et al. (1990)), or in ophiolite complexes such as the Semail ophiolite in the Oman (e.g. Stanger (1985), Kelemen and Matter (2008)). In peridotite, the concentration of Mg^{2+} is among the highest for all rocks, and this gives a good potential for carbonation processes to occur. Peridotite is therefore a promising reactant for CO_2 sequestration by mineral carbonation.

The potential of CO_2-storage in the Semail ophiolite in Oman, was calculated to be approximately 1/4 of all the CO_2 in the atmosphere if 1 wt% CO_2 were added to the peridotite (Kelemen and Matter (2008)). The main idea of in-situ carbonation is to drill into the ultramafic body and inject water saturated with CO_2 down into it.

A similar approach for in-situ CO_2-sequestration is under testing on Iceland, aiming to exploit the carbonation potential of basaltic rocks (Gislason et al. (2010)).

During carbonation of peridotite the mechanical properties of the rock will change. The bulk rock density is generally decreasing with increasing degree of serpentinization and carbonation, also leading to changes in porosity and permeability (eg. Andreani et al. (2009)). The volume increase can in turn fracture the rock and lead to an increase in the reaction rate.

To be able to make use of this natural analogue to CO_2 sequestration and industrialize it to store CO_2 on a large scale, one must understand what is controlling the rate of the reaction, and how the fracturing occurs. Rudge et al. (2010) made a simple one-dimensional model of a diffusion controlled reaction problem which induced stresses and in turn fractured the material. The article had a particular focus on how the reaction front velocity and the crack length were controlled by different parameters, and the model results were then compared with real data from the Oman ophiolite.

Chemical weathering processes are often associated with reaction induced fracturing, and there have been many studies on this problem. Yakobsen (1991) did theoretical analysis of the rate of fracturing in chemical decomposition of solids. Fletcher et al. (2006) presented a numerical study of a spheroidal weathering model. Malthe-Sørenssen et al. (2006) made a simple two-dimensional numerical model to study fractures generated by diffusion controlled volume changing reactions, and Røyne et al. (2008) presented a further development of this code to include volume increase and to compare it with field-observations of spheroidal weathering. As mentioned above, Rudge et al. (2010), made a simple 1D model of reaction-induced cracking and tested it with data for serpentinization and carbonation of peridotite.

In the Røragen-Feragen ultramafic complex in Norway, altered and fractured peridotites are exposed, and a field study was done during the Master course FYS-GEO4200/4300 given at UiO, in the autumn of 2009. An example of carbonation of peridotite is shown in Figure 1.1. Here one can see that peridotite clasts have been cemented by carbonates.

A backscattered electron (BSE) image of peridotie clasts from the Feragen ultramafic complex is shown in Figure 1.2. Quantitative chemical analyses by an electron microprobe (EMP) reveal that the minerals in the BSE image are mainly serpentine, magnesite, and olivine. One can observe that the reaction has transformed olivine to serpentine and that magnesite precipitated in the fractures. Radial fractures are observed around the olivine grain, and are possibly due to the volume expansion resulting from serpentinization and carbonation.

In this Master thesis a numerical model of diffusion controlled reaction, coupled with deformation is developed. The model of Rudge et al. (2010), is reproduced and then modified for the coupled diffusion-mechanical model developed, both in polar coordinates and in a two-dimensional Finite Element Model. By doing this we end up with a more complex stress-field in the material, and there is need

Figure 1.1: Photo from the Feragen field complex in Norway, showing carbonates (the white) cemented with clasts of peridotite (the dark).

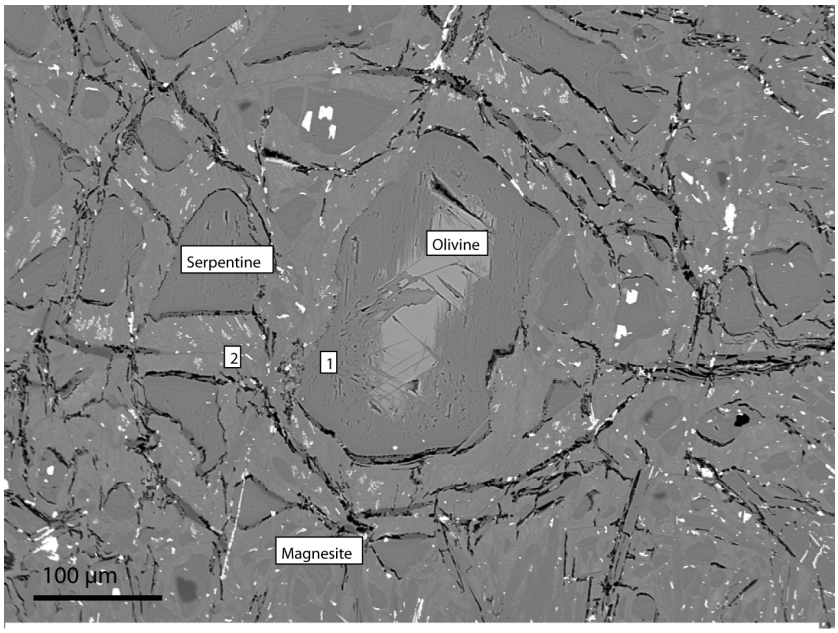

Figure 1.2: SEM from a thin section from the Feragen field complex in Norway. The number 1 and 2 are to mark that there are two different serpentine compositions in the matrix. The magnesite is found in the fractures, and appears as a dark-gray material. Total black means an open fracture.

for a different fracture criterion than that of Rudge. The two-dimensional FEM code is benchmarked using an analytical solution for thermal stress in a cylinder.

The models developed in this Master Thesis are based on natural examples, but are designed to explore the physical aspects numerically. In the second chapter the governing physical equations are motivated and discussed. The third chapter explains the basics of the numerical methods used, and in the fourth chapter the details in discretization of the physical equations are described. Benchmarking of the numerical models are shown in chapter five, together with an analytical solution of thermal stresses in a cylinder and a sphere. In chapter .. and .., stress analysis and fracture criterion are discussed, and in chapter .. results are shown and discussed.

Chapter 2

Physical problem

Chemical weathering of materials coupled to deformation is a complex problem to study. Transport of the reactants, fluid saturation, mineral reactions, changes in permeability and pore space, heterogeneities in the material, pressure and temperature, among others, are all factors that play an important role in the process of chemical weathering. If we make some simplifications, the problem can be decoupled into two different parts; one where the chemical reactions are taken into account, and one where the deformation is represented. In this chapter we will motivate simplifications and assumptions to achieve a set of equations that can model a simplified version of chemical weathering.

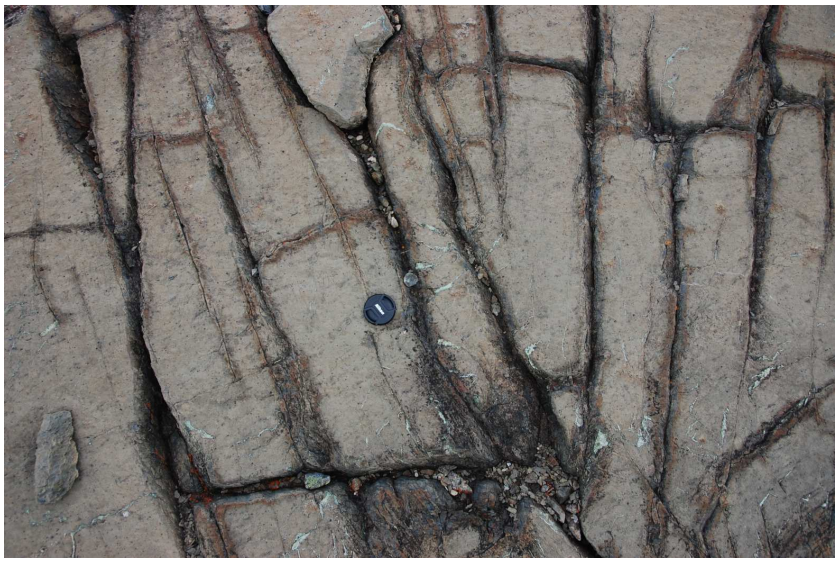

Figure 2.1: Photo from the Feragen field complex in Norway, showing a highly fractured peridotite outcrop.

2.1 Overview of chemical weathering processes

Chemical weathering of rocks occurs at the Earth's surface, and it is the process when the minerals in the rock interact with the chemicals, often dissolved in rain water or air-moisture. The most common forms of chemical weathering are oxidation, hydration, carbonation, dissolution, hydrolysis, and this project has a focus on the carbonation.

In Figure 2.1 a picture from the Feragen field complex is shown. Here one can imagine water has reacted with the rock and fractured it due to volume expansion from chemical reactions. The complex process of chemical weathering is briefly outlined in this section.

In Figure 2.2a) a sketch of rock in contact with water (e.g. rainwater) is shown. In order to make the chemicals of the water react with the minerals in the rock, the water must migrate into the rock. A rock consists of minerals and is built up by grains, and there exist pores and defects between the grains, and also inside each grain. The fluid will migrate into the rock matrix through these defects. Pressure differences, capillary pressure, diffusive-processes, etc. will transport the fluid into the rock. The migration of fluid into rocks is a slow process. In Figure 2.2b) an imaginary scenario of water diffusing inward on the grain boundaries is shown, and in Figure 2.2c) the same case is shown for pores in a single grain. These cartoons are just simple sketches of the processes, and by looking at thin-sections of rock samples in a SEM, much more complex structures are observed.

The chemical reactants are transported with the fluid, as shown in Figure 2.2d). When a fluid interacts with a rock, primary minerals may dissolve, thus changing the fluid's chemical composition. Eventually the fluid becomes saturated with respect to secondary phases, which results in precipitation. This process may take place on different scales, i.e. in the bulk fluid or in the interfacial fluid. These processes are called precipitation of solids, or dissolution in fluids, and are a delicate problem to understand, consequently a topic for many geo-chemists.

During serpentinization and carbonation of peridotite the olivine crystals are for instance reacting with the carbon dioxide in the water to form serpentinite and carbonate. The density of peridotite is higher than the density of the serpentinite and the carbonate, and if the system is closed with respect to the dominant element, the rock increases in volume, as shown in Figure 2.2e). There is a possibility that the volume increase can clog the pore space, and in that way be self limiting. Alternatively, the volume increase can cause fractures, which again opens new surfaces for the fluid to flow into and react. It is this option that is thought to be the case for serpentinization and carbonation. The process of which a rock expand during precipitation of a new mineral is a not fully understud. Although the density of the different minerals is changing there can be transport of mass out of the system, thus leading to no volume changes after all. Examples from nature show that fracturing occur, most possible due to volume expansion, but how the fracturing actually occur is not clear.

To be able to study these processes one must establish a physical model that describes the problem. In the next sections we will motivate equations for both

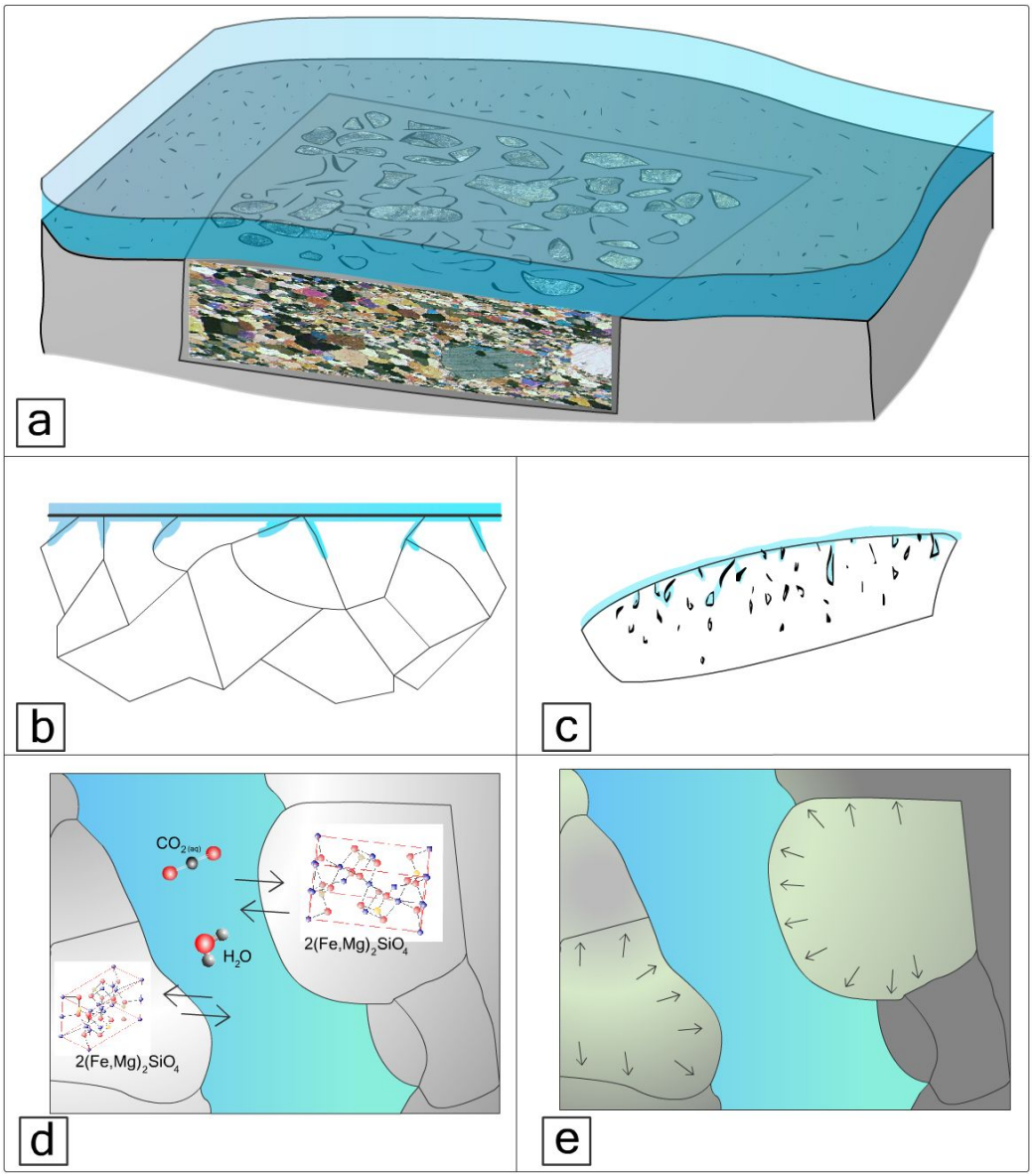

Figure 2.2: A sketch of the processes involved in chemical weathering. A rock is in contact with a thin film of water (e.g. rain water) (**a**), the water diffuses inwards along the grain boundaries(**b**) and the pores(**c**). The water transports reactants which reacts with the primary minerals in the rock(**d**), and the reaction product has a lower density and expands (**e**).

chemical reactions and the mechanical problem, and how to couple the two processes.

2.2 Equations for Chemical reactions

The reaction of peridotite to serpentine and carbonate in the presence of an aqueous phase, can be given by:

$$2Mg_2SiO_4 + CO_{2(aq)} + 2H_2O \rightarrow Mg_3Si_2O5(OH)_4 + MgCO_3 \,, \qquad (2.1)$$

where forsteritic olivine, that is the Mg member of olivine, reacts with carbon dioxide and water to produce serpentine and magnesite. This reaction is assumed to be representative for what is happening at the sea floor, where fresh mantle peridotite comes in contact with water. There are many other possible reactions that can occur when peridotite reacts with fluid, but they will not be discussed. From the reaction we can find the total molar volume before and after the reaction. From *webmineral.com* the molar masses and densities are found:

$$2 \times 43 \text{ (Forserite)} \quad \rightarrow \quad 109.5\text{(Crysotile)} \; + \; 28.1\text{(Magnesite)} \,,$$

where the unit is $\left[\frac{\text{cm}^3}{\text{mol}}\right]$. This gives a relative volume change of $\Delta V/V = 0.60$, for this idealistic reaction. Probably a more realistic value is $\Delta V/V \approx 0.30$ (Rudge et al. (2010)), but a ratio of $0.1 - 0.01$ is also within the realistic range.

Chemical reactions, such as described above, can be quantified by using a coupled diffusion-reaction problem. There have been several studies of diffusion controlled reactions, and many have used a simple diffusion equation with a rate law for the production of a reaction product (Fletcher et al. (2006), Malthe-Sørenssen et al. (2006), Røyne et al. (2008), Rudge et al. (2010)). The differences between these models are some constants and how the rate of production is defined. We choose to follow the one of Rudge et al. (2010), since their application has been directly towards carbonation and serpentinization of peridotite with respect to CO_2-storage.

First the reaction is simplified. Consider a material, A, that undergoes a chemical reaction with a surrounding fluid, W, to form a new solid material B,

$$sA + rW \rightarrow B \,,$$

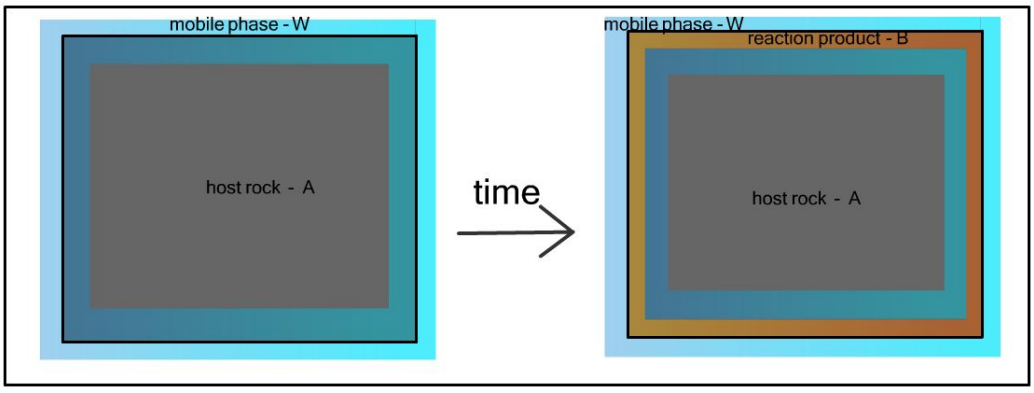

Figure 2.3: Simple model setup of the reaction-diffusion model.

where s and r are stoichiometric coefficients. The process can be described through a diffusion system where the solid product is produced at some rate, Q, depending on the concentrations of the A and W. The evolution of the concentrations of the products are described by,

$$\frac{\partial w}{\partial t} = D\frac{\partial^2 w}{\partial x^2} - rQ \tag{2.2}$$

$$\frac{\partial a}{\partial t} = -sQ \tag{2.3}$$

$$\frac{\partial b}{\partial t} = Q \tag{2.4}$$

where w is the concentration of the mobile phase W (eq. water + carbon dioxide), a is the concentration of the immobile solid A (eg.peridotite), and b is the concentration of the solid reaction result B (eg. magnesite/serpentine). The rate of production, Q, is assumed to be a simple linear rate law of the form

$$Q = kwa\ , \tag{2.5}$$

where k is a reaction rate. The dimensions of the variables are: $[w, a, b] - \frac{mol}{m^3}$, $[D] - \frac{m^2}{s}$, $[k] - \frac{m^3}{mol \cdot s}$, $[x] - m$, $[t] - s$, $[r, s] - 1$.

Further in the article of Rudge et al. (2010) it is assumed that the reaction-front propagates with a constant velocity, and that behind the front the rock is fractured and stress relaxed. Ahead of the front the water is diffusing and reacting according to these equations:

$$-v\frac{\partial w}{\partial x} = D\frac{\partial^2 w}{\partial x^2} - rQ \tag{2.6}$$

$$-v\frac{\partial a}{\partial x} = -sQ \tag{2.7}$$

$$-v\frac{\partial b}{\partial x} = Q \tag{2.8}$$

where v is the velocity of the front. This system of equations describes now a steady state situation, in the reference system of the moving reaction front. Far ahead of the front the concentration of water is assumed to be zero, together with the concentration of B, and the concentration of A is set at a level of a_0. Given in the following way,

$$w(0) = w_0 \quad w(\infty) = 0 \tag{2.9}$$

$$a(\infty) = a_0 \tag{2.10}$$

$$b(\infty) = 0 \tag{2.11}$$

A reaction rate $\kappa = skw_0$ is introduced, and also a variable $b_0 = s/a_0$, which is the value of B if all of A were reacted. From the Eqs. 2.7, 2.8, 2.10 and 2.11 it can be shown that the concentration of A is $a = s(b - b_o)$. This means that we only need to solve for w and b. The rate of production (Eq.2.5) then becomes $Q = \kappa\frac{w}{w0}(b_0 - b)$.

The reaction product B is assumed to have a lower density than the host rock material A, as when the molar volume were described above, thus a volume increase will happen when the reaction proceeds. To study the deformation set up by this volume increase we first look at the theory of elasticity.

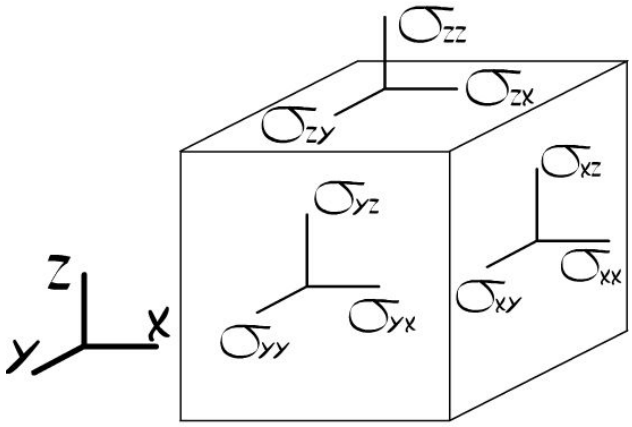

Figure 2.4: Stress components on a small volume element.

2.3 Elasticity

We choose to use the continuum approach to study the deformation related to volumetric changes from the reactions, similar to the 1D-approach of Fletcher et al. (2006), and Rudge et al. (2010). Others have used a discrete model (eg. Malthe-Sørenssen et al. (2006)), where a 2D-discrete element model with beam-interactions between nodes described the elastic material. A two dimensional finite element model is also developed in this thesis.

The physics of infinite decimal and recoverable deformation are described through the theory of elasticity (Landau and Lifshitz (1986)). For simplification purposes, plastic deformation is not consider here, although it plays a role in the deformation process.

When traction is applied to a material, and the material is not accelerating (transverse), the resulting force must vanish, and internal stress is built up in the material. Another way of producing internal stress are processes, such as thermal expansion, or in our case chemical reactions where the reaction product has a different density than the host.

In cartesian coordinates the stress on a small volume element can be expressed by three normal stress- and six shear stress-components, see Figure 2.4. Here σ_{xx} denotes the normal stress on the surface with a normal $\vec{x}$, and τ_{xy} is the shear stress on the same surface and in the direction $\vec{y}$. The stress components can be written in a matrix form, like a second-rank tensor,

$$\sigma = \begin{pmatrix} \sigma_{xx} & \tau_{xy} & \tau_{xz} \\ \tau_{yx} & \sigma_{yy} & \tau_{yz} \\ \tau_{zx} & \tau_{zy} & \sigma_{zz} \end{pmatrix}$$

The stress tensor can be shown to be symmetric.

The stress produced from applied surface- or internal-loads distort the body. The distortion can be described in terms of displacement field in the body. The relative

displacement, or the unit elongation, is called the strain. For infinite decimal deformation the strain tensor is,

$$\epsilon_{ij} = \frac{1}{2}\left(\frac{\partial u_i}{\partial x_j} + \frac{\partial u_j}{\partial x_i}\right)$$

The linear stress-strain relation yields,

$$\begin{aligned}
\epsilon_{xx} =& \frac{1}{E}\Big[\sigma_{xx} - \nu(\sigma_{yy} + \sigma_{zz})\Big] + \epsilon^* \\
\epsilon_{yy} =& \frac{1}{E}\Big[\sigma_{yy} - \nu(\sigma_{xx} + \sigma_{zz})\Big] + \epsilon^* \\
\epsilon_{zz} =& \frac{1}{E}\Big[\sigma_{zz} - \nu(\sigma_{yy} + \sigma_{xx})\Big] + \epsilon^* \,,
\end{aligned}$$

where E is Youngs modulus and is the modulus of elasticity in tension, and ν is Poisson's ratio. Both being material parameters. This relation is referred to as Hooke's law, and state that if you stretch or compress a material in one direction it will also have an effect on the other directions. The ϵ^* is often refered to as eigenstrain. For instance, for thermally induced stress it is defined as $\epsilon^* = \epsilon^T = \alpha\Delta T$.

The force balance that a small volume element must fulfill is,

$$\begin{aligned}
\frac{\partial \sigma_{xx}}{\partial x} + \frac{\partial \sigma_{xy}}{\partial y} + \frac{\partial \sigma_{xz}}{\partial z} + f_x = 0 \\
\frac{\partial \sigma_{yx}}{\partial x} + \frac{\partial \sigma_{yy}}{\partial y} + \frac{\partial \sigma_{yz}}{\partial z} + f_y = 0 \\
\frac{\partial \sigma_{zx}}{\partial x} + \frac{\partial \sigma_{zy}}{\partial y} + \frac{\partial \sigma_{zz}}{\partial z} + f_z = 0 \,,
\end{aligned} \tag{2.12}$$

where f is a force applied to the element.

2.4 Stress-strain relations for the coupled system

The coupled system is based on the stress-strain relation,

$$\sigma = D_L(\epsilon - \epsilon^*) \tag{2.13}$$

where D_L is the matrix with Lamé's parameters, ϵ is the elastic strain, and ϵ^* is the strain produced from the volume change due to the reaction. As in Rudge et al. (2010), this strain is given by,

$$\epsilon^* = \beta b / b_0 \,, \tag{2.14}$$

where β relates the amount of volume change from material A to B due to the reaction,

$$\beta = \frac{1}{3(1-\nu)}\frac{\Delta V}{V} \,,$$

b_0 is the concentration of B if all of A were reacted, $b_0 = a_0/s$.

2.5 Stress analysis

The stress state at a point in a material is fully described by the stress tensor. But the stress tensor is dependent of the coordinate system considered, and changes when the coordinate system are rotated. The eigenvalues and eigenvector of the stress tensor are independent of the coordinate system, and are thus better to use when presenting, or analyzing stress. The eigenvalue problem of the stress tensor is given by,

$$\det|\sigma_{ij} - \lambda\delta_{ij}| = 0\ .$$

Expanding the determinant gives the cubic equation for λ,

$$-\lambda^3 + \lambda^2 I_1 - \lambda I_2 + I_3 = 0\ , \tag{2.15}$$

where $I_{1,2,3}$ are the *invariants* of the stress tensor, and yields,

$$\begin{aligned} I_1 =& \sigma_{xx} + \sigma_{yy} + \sigma_{zz} \\ I_2 =& \sigma_{xx}\sigma_{yy} + \sigma_{yy}\sigma_{zz} + \sigma_{zz}\sigma_{xx} - \sigma_{xy}^2 - \sigma_{yz}^2 - \sigma_{zx}^2 \\ I_3 =& \sigma_{xx}\sigma_{yy}\sigma_{zz} + 2\sigma_{xy}\sigma_{yz}\sigma_{zx} - \sigma_{xx}\sigma_{yz}^2 - \sigma_{yy}\sigma_{zx}^2 - \sigma_{zz}\sigma_{xy}^2 \end{aligned}$$

The three eigenvalues $\lambda_{1,2,3}$ found from Equation 2.15 are called the *principal stresses*, and from them it is possible to find the eigenvectors, called the principal directions. In the coordinate system that the principal directions spand, the shear components $\sigma_{xy} = \sigma_{yz} = \sigma_{zx} = 0$, and the invariants then becomes,

$$\begin{aligned} I_1 =& \sigma_1 + \sigma_2 + \sigma_3 \\ I_2 =& \sigma_1\sigma_2 + \sigma_2\sigma_3 + \sigma_3\sigma_1 \\ I_3 =& \sigma_1\sigma_2\sigma_3 \end{aligned}$$

It is possible to decompose the stress tensor in one hydrostatic (pressure) part reflecting the mean normal stress, and one deviatoric part which represent the shear stress,

$$\sigma_{ij} = \sigma_{ij}^{dev} + \sigma_{ij}^{iso}$$

where $\sigma_{ij}^{iso} = p\delta_{ij}$, and the pressure $p = (\sigma_{11} + \sigma_{22} + \sigma_{33})/3$. The deviatoric stress is thus,

$$\sigma_{ij}^{dev} = \sigma_{ij} - p\delta_{ij} = \begin{pmatrix} \sigma_{11} - p & \sigma_{12} & \sigma_{13} \\ \sigma_{21} & \sigma_{22} - p & \sigma_{23} \\ \sigma_{31} & \sigma_{32} & \sigma_{33} - p \end{pmatrix}\ ,$$

The invariants of the deviatoric stress can be found in the same way as for the stress tensor,

$$\begin{aligned} \det|\sigma_{ij}^{dev} - \lambda\delta_{ij}| &= 0 \\ \lambda^3 - \lambda^2 J_1 - \lambda J_2 - J_3 &= 0\ , \end{aligned}$$

In stress analysis the second invariant of the deviatoric stress is often used in different failure criteria, given in terms of principal stresses,

$$J_2 = \frac{1}{6}\Big((\sigma_1 - \sigma_2)^2 + (\sigma_2 - \sigma_3)^2 + (\sigma_3 - \sigma_1)^2\Big)\ .$$

The magnitudes of the principal stresses are defined as $\sigma_1 \geq \sigma_2 \geq \sigma_3$.

The octahedral stress is defined as the resultant shear stress on a plane that makes the same angle with the three principal directions (Westergaard (1964)). The octahedral stress can be expressed in terms of the second invariant of the deviatoric stress,

$$\tau_{oct}^2 = \frac{2}{3} J_2 \ .$$

The Von Mises stress is also defined from the second invariant of the deviatoric stress,

$$\sigma_v = \sqrt{3 \ J_2} \ ,$$

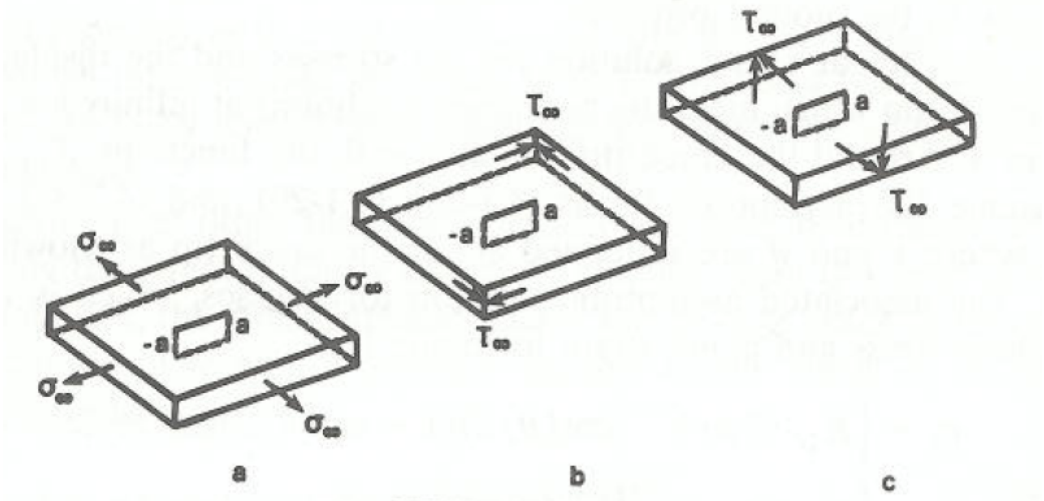

Figure 2.5: The different modes of fracture. (Unger (2001))

2.6 Basics of Fracture Mechanics

In linear elastic fracture mechanics it is normal to talk about three different modes of fracture when addressing the problem of loading a plate with an internal crack (Unger (2001)). The different modes are related to different ways of loading the plate. Mode I is referred to the case when tensile forces are applied perpendicular to the two crack surfaces in order to propagate the fracture. Mode II fracturing occur if in-plane shear forces are applied to a body containing a crack. Mode III is the case with out-of-plane shear forces acting on the plate, also called tearing mode of fracture. See Figure 2.5 for examples of the different modes. Away from a crack-tip the stress decays proportionally with $1/\sqrt{r}$.

2.6.1 Coulomb criterion

The strength of materials can be determined from laboratory experiments, for instance one can measure the uniaxial compressive strength or the uniaxial tensile strength with the use of a device that can stretch or compress the a sample in the axial direction. The uniaxial compressive strength is defined as (Pollard and Fletcher (2005)),

$$C_u = \left|\sigma_a(\min)\right| \quad \sigma_1 > 0, \quad \sigma_2 = \sigma_3 = 0\,,$$

and the uniaxial tensile strength like,

$$T_u = \sigma_a(\max) \quad \sigma_1 = \sigma_2 = 0, \quad \sigma_3 < 0\,,$$

where the stress is positive for tension and negative for compression. The stress σ_a is the axial stress at failure. The units are the same as for stress $[T_u, C_u]$ = Pa, and are typically of orders MPa for rocks.

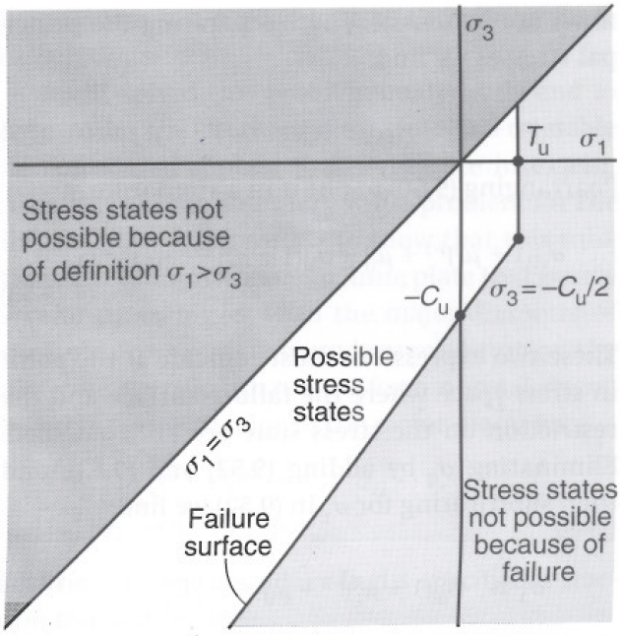

Figure 2.6: The principal stress space with the Coulomb failure surface plotted. (Pollard and Fletcher (2005), Fig 9.25)

Examples from nature and laboratory studies often show that shear fracturing occur in brittle materials. If the principal stresses are known, the maximum shear stress is found to be $\sigma_s = \frac{1}{2}|\sigma_1 - \sigma_3|$, hence independent of the intermediate stress σ_2. The maximum shear *strength* is defined as (Pollard and Fletcher (2005)),

$$S_m = \sigma_s(\max), \quad \sigma_1 > \sigma_3$$

The criterion of Coulomb (1773) suggest that the maximum shear stress at failure relates to material parameters like,

$$|\sigma_s| = S_0 - \mu_i \sigma_n, \quad \sigma_1 < T_u$$

where σ_n is the normal stress on the plane of failure, S_0 is the cohesion, or the inherent shear strength of the material and μ_i is the internal friction coefficient. The Coulomb criterion is used to define the Coulomb stress σ_C as,

$$\sigma_C = |\sigma_s| + \mu_i \sigma_n, \quad \sigma_1 < T_u \text{ and } \sigma_C \leq S_0 \ .$$

If one makes use of the critical Coulomb angle γ_c, that is the angle between the major principal and the potential shear fracture surface, it is possible to derive the relation for the critical Coulomb stress (Pollard and Fletcher (2005)),

$$\sigma_{CC} = \frac{1}{2}(\sigma_1 - \sigma_3)(1 + \mu_i^2)^{1/2} + \frac{1}{2}(\sigma_1 + \sigma_3)\mu_i \ , \tag{2.16}$$

with the restrictions $\sigma_1 < T_u$ and $\sigma_{CC} \leq S_0$.

When failure occurs in both tension and shear it is possible to draw the failure surface in the principal stress space. From the expression of the critical Coulomb

stress in Eq. 2.16, the Coulomb criterion as a failure surface can be defined, and setting $\sigma_{CC} = S_0$, gives (Pollard and Fletcher (2005)),

$$\begin{aligned}\sigma_3 &= -2S_0\left[(1+\mu_i^2)^{1/2}+\mu_i\right] + \left[\frac{(1+\mu_i^2)^{1/2}+\mu_i}{(1+\mu_i^2)^{1/2}-\mu_i}\right]\sigma_1 \,, \\ &= -C_u + \left[(1+\mu_i^2)^{1/2}+\mu_i\right]^2\sigma_1 \,, \end{aligned} \tag{2.17}$$

where C_u is the uniaxial compressive strength, and μ_i is the internal friction coefficient, both being material parameters. The failure surface is plotted in the principal stress space in Figure 2.6.

The Coulomb criterion is a semi-empirical law, mostly based on observations and experiments.

2.6.2 Energy balance

Griffith (1920) considered the energy balance if a crack was initiated/propagating. He argued with that the energy used to open new fractures, should be equal to the surface energy of the new opened surfaces. The mechanical energy release rate was defined like (Hellan (1984)),

$$\mathcal{G} = 2\gamma \,,$$

where γ is the surface energy of one of the new opened surfaces.

The criterion for crack propagation,

$$\mathcal{G} > \frac{dU_s}{dc}$$

where U_s is the surface energy, and c is the inital crack length/ flaw size.

For instance Fletcher et al. (2006) used this approach when setting up a fracture criterion. They assumed that as a chemical reaction proceeded, a reaction product precipitated which had a different volume, and elastic strain energy build up. A fracture was assumed to form if the elastic strain energy per unit area was equal to the surface energy of the fracture, 2Γ,

$$\int U(x)dx = 2\Gamma \,.$$

2.6.3 Stress intensity factor

The stress-state at a crack-tip can be given by the stress intensity factor K. For the different modes of fracture this factor is,

$$\begin{aligned} \text{Mode I} \quad & K = \sigma_\infty(\pi a)^{1/2} \\ \text{Mode II} \quad & K = \tau_\infty(\pi a)^{1/2} \\ \text{Mode III} \quad & K = \tau_\infty(\pi a)^{1/2} \end{aligned}$$

where a is the fracture length as shown in Figure 2.5, where also the three different modes of fracture are shown. For different geometries than the ones shown in the figure, the stress intensity factor varies with some prefactor, and it is possible to make analytical predictions for many different cases (Tada et al. (1973)).

2.6.4 Fracture criterion used in the model of Rudge et al. (2010)

In the model of Rudge et al. (2010), there is proposed a fracture criterion based on the stress intensity factor approach. The numerical prefactor due to geometry, and numerical prefactors such as π, are not taken into account as the main goal is an overall scaling. The stress intensity factor of Rudge et al. (2010), is thus

$$K = \sigma L^{1/2}$$

where L is the fracture length. Furthermore the steady state assumption previously mentioned, give rise to the assumption that the stress intensity factor always is at its critical value K_c. The crack length L is assumed to be the length for which the stress is reduced by a factor of $1/e$ from its value at the front. The strain induced by the volume change is defined in Eq. 2.14, and the stress is defined as Youngs modulus times the strain, $\sigma = E\beta b/b_0$. The stress intensity factor becomes then,

$$K = E\beta \frac{b}{b_0} L^{1/2} \,, \tag{2.18}$$

and L is shown in Figure 2.7.

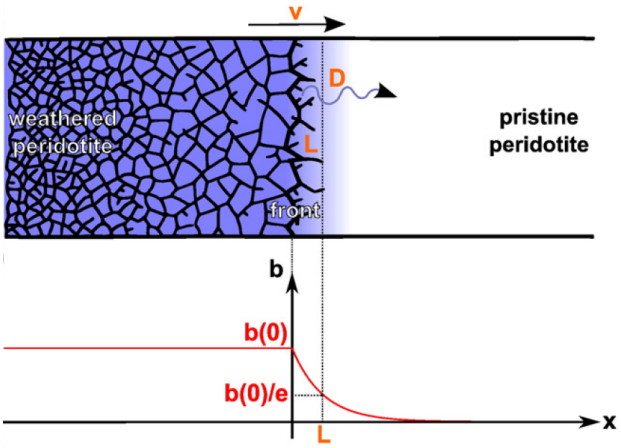

Figure 2.7: Setup showing the model setup. (Rudge et al. (2010) Fig. 1)

Chapter 3

Methods

In order to study the physical problem, mathematical equations were motivated in the previous chapter. To solve a mathematical equation it is two main possibilities, either by analytical- or numerically calculations. Analytical solutions are often not available due to difficult boundaries, or inhomogenities in the problem, and therefore numerical methods are used. In this project we will solve the partial differential equations (PDE's) numerically, and test the results with an analytical solution to a simplified problem. The numerical methods we will use is the finite difference method (FDM), and the finite element method (FEM). The models will be implemented in Matlab.

In this chapter the basics of the methods will be gone through using a simple diffusion problem as an example,

$$\frac{\partial T(t,x)}{\partial t} = \kappa \frac{\partial^2 T(t,x)}{\partial x^2} \,, \tag{3.1}$$

where $x \in [x_a, x_b]$, and $t \in [t_0, t_1]$. The boundary conditions are set to: a Dirichlet boundary condition on one side, $T(x_a, t) = 1$, and a flux boundary condition on the other $\frac{dT}{dx}|_{x_b} = 0$. The initial value of T is set to zero inside the domain. The function T can represent any given quantity, for example temperature.

3.1 Basics of the Finite Difference method

The finite difference method are approximating the functions on a discrete grid. The domain in the example-problem above can be discretized in the following way: $x_i = x_a + i\Delta x$, where $i = 1, 2, ..., n_x$ and $\Delta x = (x_b - x_a)/n_x$, in space, and $t_i = t_0 + l\Delta t$, where $l = 1, 2, ..., n_t$ and $\Delta t = (t_1 - t_0)/n_t$, in time. For the variable we then get, $T(x,t) = T(x_a + i\Delta x, t_0 + l\Delta t) = T_i^l$. In Figure 3.1 the discretization is shown.

The derivatives in Eq.3.1 are approximated using Taylor series expansions of the function values. The derivative for the value T_i, can be approximated like,

$$T_{i+1} = T_i + \Delta x \frac{\partial T}{\partial x}\Big|_i + \frac{\Delta x^2}{2}\frac{\partial^2 T}{\partial x^2}\Big|_i + \frac{\Delta x^3}{6}\frac{\partial^3 T}{\partial x^3}\Big|_i + \cdots \,,$$

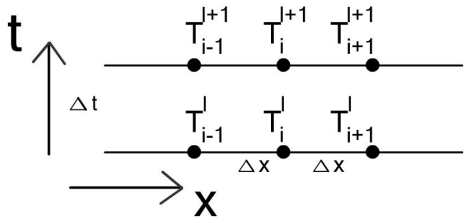

Figure 3.1: Discrete points in a 1D domain with time dependence.

truncate the terms of second order and higher, divide by Δx, and move the first derivative term to the right hand-side,

$$\frac{\partial T}{\partial x}\Big|_i = \frac{T_{i+1} - T_i}{\Delta x} + O(\Delta x) \,, \tag{3.2}$$

where $O(\xi^m)$ is the truncation error of order m, that we get by doing the approximation. The Taylor series expansion can also be done for the funtion value in the discrete point one step back,

$$T_{i-1} = T_i - \Delta x \frac{\partial T}{\partial x}\Big|_i + \frac{\Delta x^2}{2}\frac{\partial^2 T}{\partial x^2}\Big|_i - \frac{\Delta x^3}{6}\frac{\partial^3 T}{\partial x^3}\Big|_i + \cdots$$

we do the same truncation here, and divide by Δx, to obtain

$$\frac{\partial T}{\partial x}\Big|_i = \frac{T_i - T_{i-1}}{\Delta x} + O(\Delta x) \,. \tag{3.3}$$

By subtracting the two entire series from each other,

$$\begin{aligned} T_{i+1} - T_{i-1} &= 2\Delta x \frac{\partial T}{\partial x}\Big|_i + O(\Delta x^3) \\ \frac{\partial T}{\partial x}\Big|_i &= \frac{T_{i+1} - T_{i-1}}{2\Delta x} + O(\Delta x^2) \,, \end{aligned} \tag{3.4}$$

one obtain yet a different way of approximating the derivative of the function value T in point x_i. This has also a higher order truncation error.

These schemes are called respectively the forward Euler in Eq.3.2, the backward Euler in Eq.3.3, and the centred difference scheme in Eq.3.4.

For the second order derivative in space, we use the centred difference scheme twice, and by using half-step ($T_{i+1/2}$) for each derivative, we get,

$$\frac{\partial^2 T}{\partial x^2}\Big|_i \approx \frac{T_{i+1} - 2T_i + T_{i-1}}{\Delta x^2}$$

The example problem in Eq. 3.1, can be approximated with the centred difference scheme in space, and an *explicit* time scheme for in time,

$$\frac{T_i^{l+1} - T_i^l}{\Delta t} = \kappa \frac{T_{i+1}^l - 2T_i^l + T_{i-1}^l}{\Delta x^2} \quad \text{Forward} \,.$$

Explicit schemes uses only values *explicitly* given from the previous time step to update the next step.

Using an *implicit* scheme in time gives,

$$\frac{T_i^{l+1} - T_i^l}{\Delta t} = \kappa \frac{T_{i+1}^{l+1} - 2T_i^{l+1} + T_{i-1}^{l+1}}{\Delta x^2} \quad \text{Backward .} \tag{3.5}$$

Implicit schemes are solved by using a set of linear equations. For the case in equation 3.5, we end up with the system,

$$T_i^{l+1}\left(1 + 2\kappa\frac{\Delta t}{\Delta x^2}\right) - \kappa\frac{\Delta t}{\Delta x^2}T_{i+1}^{l+1} - \kappa\frac{\Delta t}{\Delta x^2}T_{i-1}^{l+1} = T_i^l \ ,$$

or in a matrix-vector notation,

$$\begin{pmatrix} & & & & \\ . & . & . & & \\ 0 & -1s & (1+2s) & -1s & 0 \\ & & . & . & . \\ & & & & \end{pmatrix} \begin{pmatrix} \\ \\ T_i^{l+1} \\ \\ \\ \end{pmatrix} = \begin{pmatrix} \\ \\ T_i^l \\ \\ \\ \end{pmatrix} ,$$

where $s = \kappa\frac{\Delta t}{\Delta x^2}$. To set up the full system of equations, boundary conditions are needed, and these are given after Eq.3.1, and were one Dirichlet-, and one flux boundary conditions. The flux boundary needs to be treated first. We can approximate the derivative at the boundary node using a centred difference scheme,

$$\frac{dT_b}{dx} \approx \frac{T_{n+1} - T_{n-1}}{2\Delta x} = 0 \quad \Longrightarrow \ T_{n+1} = T_{n-1} \ ,$$

and the equation for the boundary node becomes, $-2s(T_{n-1}^{l+1}) + (1+2s)T_n^{l+1} = T_n^l$. This gives the full system of equations,

$$\begin{pmatrix} (1+2s) & -1s & 0 & . & . & & \\ -1s & (1+2s) & -1s & . & . & & \\ 0 & -1s & . & . & . & & \\ . & . & . & . & & & \\ & & & & & -1s & \\ & & & & -2s & (1+2s) & \end{pmatrix} \begin{pmatrix} T_2^{l+1} \\ \\ \\ \\ \\ T_n^{l+1} \end{pmatrix} = \begin{pmatrix} T_2^l + sT_1^{l+1} \\ \\ \\ \\ \\ T_n^l \end{pmatrix} ,$$

If we name the matrix A and the known right hand side vector b, we have the system $AT = b$, where T are the unknown.

In the models developed in this thesis, we will use a *sparse* storage of the matrices. That is to only store the non-zero entries in the matrix, and in that way reduce the amount of storage needed on a computer. Since the matrix above only has non-zero entries on the three diagonals, the number of zeros is very high, and we gain a lot using a sparse storage.

To solve the system of equations we will simply use the method provided by Matlab in the 'backslash' operator. This runs first through many test to find out the structure of the matrix and then use the appropriate solver.

3.2 Basics of the Finite Element Method

The diffusion problem given in Eq.3.1, is dependent on both time and space. The time-dependence in a PDE is normally treated with a finite difference approximation. Thus we have $T(t,x) \approx T^l(x) = T(t_0 + \Delta t\ l, x)$, for the discretized function in time, and we use a implicit difference scheme for the temporal derivative,

$$\frac{T^{l+1}(x) - T^l(x)}{\Delta t} = \kappa \frac{\partial^2 T^{l+1}(x)}{\partial x^2}$$

The spatial part of the function is approximated with a number of prescribed shape- or interpolating functions, N_i, in the following way,

$$T^l(x) \approx \hat{T}^l(x) = \sum_{j=1}^{n} T_j^l N_j(x)\ , \tag{3.6}$$

where the T_j are the unknown coefficients we want to solve for, and the ultimate goal is to compute T_j such that the error $T - \hat{T}$ is minimized (Langtangen (2003)). There are n number of shape-functions for the n computational nodes.

The shape-functions must have the property of being orthogonal, they should divide the computational domain into non-overlapping elements, and they must satisfy the boundary conditions exactly. They can for instance be sets of polynomials, sine-Fourier series, or some combination. The shape functions using Lagrangian polynomials are for instance given by,

$$N_i(x) = \frac{\Pi_{k \neq i}(x - x_k)}{\Pi_{k \neq i}(x_i - x_k)}\ ,$$

where the polynomials have the property $N_i(x_k) = \delta_{ik}$, where δ is the Kronecker-delta.

The boundary conditions to our example problem were given after Eq.3.1 in the beginning of this chapter. There were one Dirichlet boundary at $x = x_a$, namely $T(x_a, t) = 0$, and one flux boundary condition at $x = x_b$, $\frac{dT}{dx}|_{x_b} = 0$. The shape functions introduced in Eq. 3.6 must fulfil these conditions. The Dirichlet boundary condition sets the restriction on N that $N_i(x_a) = 0$. The flux boundary condition, also called Neumann, comes into the formulation when integration by parts is performed later.

For one-dimensional problems one can choose different order of elements, where first order elements have only two nodes and linear shape-functions, while second order elements have three nodes and quadratic shape-functions.

For two-dimensional problems the most common elements are triangles or quads. It is the number of nodes in the element which gives the order of the shape functions. In the two-dimensional code developed in this Master thesis only triangles are used, therefore triangles are the only 2D elements discussed further. For a three-node triangle, linear shape-functions are used, and for a six-node

Table 3.1: Shape-functions for triangles of 3- and 6-node.

Linear 3-node triangular	Quadratic 6-node triangular	
$N_1 = 1 - u - v = w$	$N_1 = w(2w-1)$	$N_4 = uv$
$N_2 = u$	$N_2 = u(2u-1)$	$N_5 = vw$
$N_3 = v$	$N_3 = v(2v-1)$	$N_6 = uw$

triangle quadratic shape-functions are used. In Figure 3.3 a three-node and a six-node triangular element are shown.

The shape-functions for the two type of triangles used in our model, are given in the table 3.1.

The operator called residual, is for our example-problem defined by

$$R(T) = \frac{T^{l+1}(x) - T^{l}(x)}{\Delta t} - \kappa \frac{\partial^2 T^{l+1}(x)}{\partial x^2}$$

The residual is zero if an analytical solution would be inserted $R(T_{\text{analytical}}) = 0$, but with the discretized function it will differ from zero $R(\hat{T}) \neq 0$.

The Weighted Residual method (Fletcher (1984)) applies a weighted mean of R over the computational domain,

$$\int_{\Omega} R(\hat{T}) W_i \, d\Omega = 0 \, , \quad i = 1, ..., n \, .$$

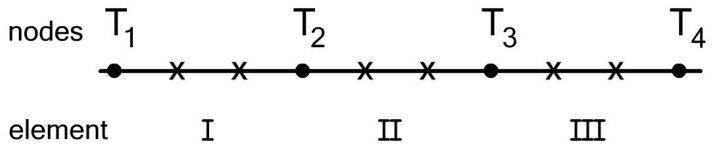

Figure 3.2: Elements in a 1D domain, shows three 4-nodes elements. The nodes denoted with T_1, ... , T_4 is the global nodes, and for each of the three elements there exists four local nodes.

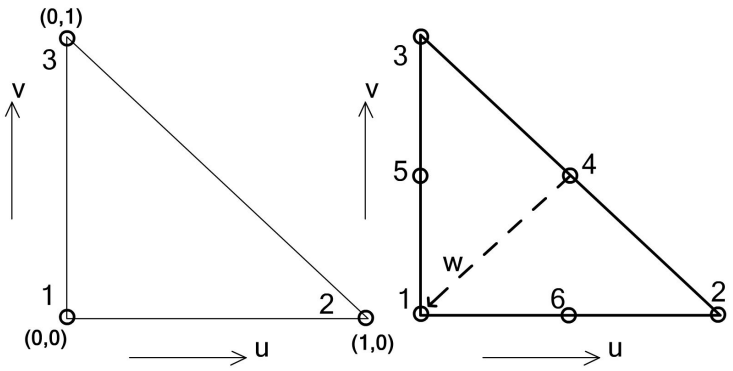

Figure 3.3: The 3- and 6-node triangulare element, in the reference coordinates.

where the main goal is to find the nodal unknowns T_j such that this integral becomes zero for n linearly independent weigthing functions.

If the sets of the shape functions N_i, and the weigthing functions W_i are chosen to be equal, the method is called the Galerkin Finite Element method. On the weak formulation of the PDE, that is the integral form, we get for our example problem,

$$\int_{x_a}^{x_b} \left(\hat{T}^{l+1}(x) - \Delta t \kappa \frac{\partial^2 \hat{T}^{l+1}(x)}{\partial x^2} \right) N_i(x)\, dx = \int_{x_a}^{x_b} T^l(x) N_i(x)\, dx\,, \quad i = 1, ..., n\,,$$

where we have rearranged to get the unknowns on the left hand side, and on the right hand side the known T^l. Integration by parts is performed on the partial derivative-term, to get

$$\int_{x_a}^{x_b} \hat{T}^{l+1}(x) N_i(x) + \Delta t \kappa \frac{\partial \hat{T}^{l+1}(x)}{\partial x} \frac{\partial N_i(x)}{\partial x}\, dx = \int_{x_a}^{x_b} T^l(x) N_i(x)\, dx + N_i(x_b) T'(x_b) - N_i(x_a) T'(x_a)\,. \quad i = 1, ..., n\,, \tag{3.7}$$

As discussed above, the Dirichlet boundary condition forced $N_i(x_a) = 0$. The flux-boundary at $x = x_b$ gives $T'(x_b) = 0$. We now insert for the $\hat{T}^l(x) = \sum_{j=1}^{n} T_j^l N_j(x)$,

$$\sum_{j=1}^{n} T_j^{l+1} \int_{x_a}^{x_b} N_j(x) N_i(x) + \Delta t \kappa \frac{\partial N_j(x)}{\partial x} \frac{\partial N_i(x)}{\partial x}\, dx = \int_{x_a}^{x_b} T^l(x) N_i(x)\, dx\,. \quad i = 1, ..., n\,.$$

This linear system of equation can be written in a matrix vector notation like $AT = b$, where

$$A_{i,j} = \int_{x_a}^{x_b} N_j(x) N_i(x)\, dx + \int_{x_a}^{x_b} \Delta t \kappa \frac{\partial N_j(x)}{\partial x} \frac{\partial N_i(x)}{\partial x}\, dx = M_{i,j} + \Delta t \kappa K_{i,j}$$

and $b_i = \int_{x_a}^{x_b} T^l(x) N_i(x)\, dx$. The matrix M is called the mass-matrix, and K is called the stiffness matrix.

Before the full system of equation can be solved in the same manner as for the FDM, the derivatives of the shape-functions and the integration over the domain

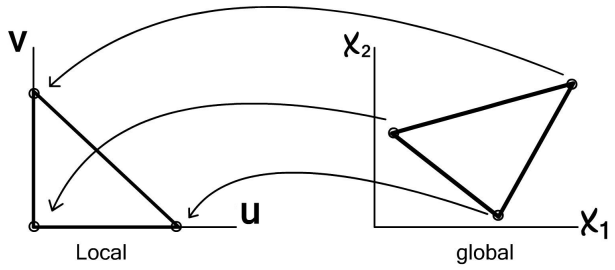

Figure 3.4: Mapping from global to local element for a linear triangulare element.

Table 3.2: Gaussian integration points for triangles in frame of reference.

w	ip_u	ip_v	ip_w
3 point formula. Degree of precision 2			
0.33333 33333 33333	0.50000 00000 00000	0.50000 00000 00000	0.00000 00000 00000
6 point formula. Degree of precision 4			
0.10995 17436 55322	0.81684 75729 80459	0.09157 62135 09771	0.09157 62135 09771
0.22338 15896 78011	0.10810 30181 68070	0.44594 84909 15965	0.44594 84909 15965

needs to be performed. The way this is done is by mapping each element to a reference element, where in one-dimensions this is between -1 and 1, and the performe the integration by Gauss integration point rule. After the integration is performed the element matrices are assembled onto the global matrix, and the full linear system of equations is solved.

For the two-dimensional case the mapping of a triangle onto a reference element, is shown in Figure 3.4. When derivation of the function is performed in the reference element, we have

$$\begin{pmatrix} \frac{dT}{dx} \\ \frac{dT}{dy} \end{pmatrix} = \begin{pmatrix} \frac{du}{dx} & \frac{dv}{dx} \\ \frac{du}{dy} & \frac{dv}{dy} \end{pmatrix} \begin{pmatrix} \frac{dT}{du} \\ \frac{dT}{dv} \end{pmatrix},$$

where the matrix is the called the Jacobian.

Integration of a function $f(u, v)$ over a reference triangular element is done in the following way,

$$\int_\Omega f(u,v)dudv \approx \sum_{i=1}^{nip} f(u_i, v_i) ip_w$$

where the integration points, ipu and ipv, and weigths ipw are given in Table 3.2.

For mesh generation, the Triangle mesh generator (Shewchuk (2005)) is used. It produces an unstructured mesh of triangles using constrained Delaunay technique.

Chapter 4

Discretization

In this chapter the methods discussed in the previous chapter are used to discretize the mathematical equations of the physical problem found in Chapter 2.

- The one-dimensional steady state reaction-diffusion problem of Rudge et al. (2010), given in Eq. 2.6-2.8, is discretized using the FDM.
- The time dependent reaction-diffusion problem in Eq. 2.2-2.5, coupled with the mechanical problem in Eq. 2.12, and 2.13, are discretized using FEM in two dimensions,
- the same problem is also rewritten in polar coordinates and discretized using the FDM.

4.1 Steady state reaction-diffusion problem

The steady state reaction-diffusion problem proposed by Rudge et al. (2010), given in Eq. 2.6 and 2.8 yields,

$$-v\frac{\partial w}{\partial x} = D\frac{\partial^2 w}{\partial x^2} - rQ\,, \tag{4.1}$$

$$-v\frac{\partial b}{\partial x} = Q\,. \tag{4.2}$$

To make it easier to solve, the Eq. 4.2 is inserted in Eq. 4.1, and then integrated over x once,

$$\frac{\partial w}{\partial x} = -v\big(w + rb\big)/D\,, \tag{4.3}$$

$$\frac{\partial b}{\partial x} = -\frac{1}{v}\kappa\frac{w}{w_0}(b_0 - b)\,, \tag{4.4}$$

where the rate of production Q is inserted by $Q = \kappa \frac{w}{w_0}(b_0 - b)$. The boundary conditions given in Equations 2.9 and 2.11 were

$$w(0) = w_0 \quad w(L) = 0 \,, \tag{4.5}$$

$$b(L) = 0 \,, \tag{4.6}$$

where instead of $w, b(\infty)$ we have inserted L, a finite domain size.

The concentration of W and B are discretized using the FDM, $w(x) = w(i\Delta x)$ and $b(x) = b(i\Delta x)$, for $i = 1, 2, ..., nx$. Given the boundary conditions, we can use a forward Euler scheme for w, and a backward Euler scheme for b,

$$\begin{aligned} \frac{w_i - w_{i-1}}{\Delta x} &= -v\big(w_{i-1} + rb_{i-1}\big)/D \\ \implies w_i &= w_{i-1} - \Delta x\, v\big(w_{i-1} + rb_{i-1}\big)/D \end{aligned} \tag{4.7}$$

$$\begin{aligned} \frac{b_i - b_{i-1}}{\Delta x} &= -\frac{1}{v}\kappa \frac{w_i}{w_0}(b_0 - b_i) \\ \implies b_{i-1} &= b_i + \Delta x \frac{1}{v}\kappa \frac{w_i}{w_0}(b_0 - b_i) \,. \end{aligned} \tag{4.8}$$

We use an iterative method, called the relaxation method, where the difference between the updated w and the old w_{old}, $\Delta w = w - w_{\text{old}}$, is weigthed with a number $\alpha < 1$. To get convergence α must be chosen sufficiently small, however the number of iterations needed to reach a steady state is dependent on α, and this should not be to many to keep the computational time low. The algorithm is thus,

---

w(1) = w0;
b(end) = 0;
Loop over number of iterations
    w_{old} = w;
    Loop over w. From 2 to (nx-1)
        $w_i = \frac{1}{2}\Big[w_{i+1} + w_{i-1} - \frac{\Delta x^2}{D} r\, \kappa\, \frac{w_{i-1}}{w0}\, (b0 - b_{ix-1}) ...$
        $+ v\, \frac{\Delta x}{D}\, (w_i - w_{i-1}) \Big]$;
    $w = w_{\text{old}} + \alpha\, (w - w_{\text{old}})$;
    Loop over b. From nx to 2
        $b_{i-1} = b_i + \frac{dx}{v}\kappa\, \frac{w_i}{w0}(b0 - b_i)$;

Algorithm 4.1: The relaxation method is used to find the steady state in the reaction-diffusion model.

4.2 The coupled transient reaction-diffusion and mechanical problem in 2D using FEM

The discretization of the coupled 2D problem is performed using FEM, employing an unstructured triangular computational mesh (Shewchuk (2005)).

In this section we will go through the discretization of first the diffusion-reaction model, and then the coupled mechanical model.

4.2.1 Diffusion-reaction model in two-dimensions

The reaction-diffusion model proposed by Rudge et al. (2010), is given in the Eqs. 2.2-2.4. In a more general form this yields,

$$\frac{\partial w(\mathbf{x},t)}{\partial t} = \nabla\left(D(\mathbf{x},t)\nabla w(\mathbf{x},t)\right) - rkw(\mathbf{x},t)a(\mathbf{x},t) \tag{4.9}$$

$$\frac{\partial a(\mathbf{x},t)}{\partial t} = -skw(\mathbf{x},t)a(\mathbf{x},t) \tag{4.10}$$

$$\frac{\partial b(\mathbf{x},t)}{\partial t} = kw(\mathbf{x},t)a(\mathbf{x},t) \tag{4.11}$$

where the rate of production $Q = ka(\mathbf{x},t)w(\mathbf{x},t)$ is already inserted.

We use the FDM discretization for the temporal part, $w(\mathbf{x},t) = w(\mathbf{x},t_0 + l\Delta t) = w(\mathbf{x})^l$, and similar for a and b, and a implicit scheme on the temporal derivative,

$$\frac{w(\mathbf{x})^l - w(\mathbf{x})^{l-1}}{\Delta t} = \nabla\left(D(\mathbf{x})^l\nabla w(\mathbf{x})^l\right) - rkw(\mathbf{x})^l a(\mathbf{x})^l \tag{4.12}$$

$$\frac{a(\mathbf{x})^l - a(\mathbf{x})^{l-1}}{\Delta t} = -skw(\mathbf{x})^l a(\mathbf{x})^l \tag{4.13}$$

$$\frac{b(\mathbf{x})^l - b(\mathbf{x})^{l-1}}{\Delta t} = kw(\mathbf{x})^l a(\mathbf{x})^l \tag{4.14}$$

The spatial derivative in Eq. 4.12 can now be discretize using the Galerkin finite element method. Following the procedure described in Chapter 3, we first multiply with a weigthing function $N(\mathbf{x})$ and then integrate over domain, to obtain the weak formulation of the PDE,

$$\int_\Omega N(\mathbf{x})\left(w(\mathbf{x})^l - w(\mathbf{x})^{l-1}\right)d\Omega = \Delta t\int_\Omega N(\mathbf{x})\left(\nabla\left(D(\mathbf{x})^l\nabla w(\mathbf{x})^l\right) - rkw(\mathbf{x})^l a(\mathbf{x})^l\right)d\Omega$$

where the functions N belong to a infinite set of weigthing functions. We rewrite to get the unknowns on the left hand side,

$$\int_\Omega w(\mathbf{x})^l N(\mathbf{x}) - \Delta t\nabla\left(D(\mathbf{x})^l\nabla w(\mathbf{x})^l\right)N(\mathbf{x}) + \Delta trkw(\mathbf{x})^l a(\mathbf{x})^l N(\mathbf{x})d\Omega = \int_\Omega N(\mathbf{x})w(\mathbf{x})^{l-1}d\Omega$$

Integration by parts, and Greens lemma[1], are performed on the mid-term on the left hand side,

$$\int_\Omega w(\mathbf{x})^l N(\mathbf{x}) + \Delta t D(\mathbf{x})^l \nabla w(\mathbf{x})^l \nabla N(\mathbf{x}) + \Delta t r k w(\mathbf{x})^l a(\mathbf{x})^l N(\mathbf{x}) d\Omega = \int_\Omega N(\mathbf{x}) w(\mathbf{x})^{l-1} d\Omega + \int_{\delta\Omega} \Delta t D(\mathbf{x})^l \frac{\partial w(\mathbf{x})^l}{\partial \vec{n}} N(\mathbf{x}) d\Gamma$$

where the integral over $\delta\Gamma$ is the curve integral over the boundary $\delta\Omega$, arising from Greens lemma.

The fields w, a, and b are approximated by a linear combination of shape functions,

$$w^l(\mathbf{x}) \approx \hat{w}^l(\mathbf{x}) = \sum_j^{nnod} w_j^l N_j(\mathbf{x})$$

where nnod is the number of nodes in the computational domain. The weigthing function $N(\mathbf{x})$ is the same as the shape functions because we are using the Galerkin FEM. Inserting for the approximation of w gives

$$\sum_j^{nnod} w_j^l \int_\Omega N_i N_j d\Omega + \Delta t \sum_j^{nnod} w_j^l \int_\Omega r k N_i N_j a(\mathbf{x})^l d\Omega + \Delta t \sum_j^{nnod} w_j^l \int_\Omega \nabla N_i D^l \nabla N_j d\Omega = \int_\Omega w^{l-1} N_i d\Omega + \Delta t \int_{\delta\Omega} D^l \frac{\partial w(\mathbf{x})^l}{\partial \vec{n}} N_i d\Gamma \ , \quad i = 1, 2, ..., \text{nnod}$$

where the right hand side is known. The system of equations can be rewritten if matrix notation is introduced,

$$\sum_j^{nnod} w_j^l \Big(M_{i,j} + r k \Delta t G_{i,j} + \Delta t K_{i,j} \Big) = f_i \ , \quad i = 1, 2, ..., \text{nnod} \tag{4.15}$$

where M is the so called mass matrix, $M_{i,j} = \int_\Omega N_i N_j d\Omega$, K is the stiffness matrix, $K_{i,j} = \int_\Omega \nabla N_i \nabla N_j d\Omega$, and G are a modified version of the mass matrix, $G_{i,j} = \int_\Omega N_i N_j a(\mathbf{x})^l d\Omega$. The right hand side vector is $f_i = \int_\Omega w^{l-1} N_i d\Omega + \Delta t \int_{\delta\Omega} D^l \frac{\partial w(\mathbf{x})^l}{\partial \vec{n}} N_i d\Gamma$.

The same procedure is then done for the concentrations a and b. When Eq. 4.13 is multiplied with a weigthing function and integrated over the domain, it yields,

$$\int_\Omega N_i a(\mathbf{x})^l (1 + \Delta t k w(\mathbf{x})^l) d\Omega = \int_\Omega N_i a(\mathbf{x})^{l-1} d\Omega \ , \quad i = 1, 2, ..., \text{nnod}$$

and similar for Eq. 4.14 for b,

$$\int_\Omega N_i b(\mathbf{x})^l d\Omega = \int_\Omega N_i b(\mathbf{x})^{l-1} d\Omega - \Delta t k \int_\Omega N_i w(\mathbf{x})^l a(\mathbf{x})^l d\Omega \ , \quad i = 1, 2, ..., \text{nnod}$$

As described above the concentrations are approximated by a linear combination of shape-functions, and we use the same set of functions used for w. In the end

[1]Greens lemma states that: $\int_\Omega \nabla \big(c \nabla u(\mathbf{x}) \big) v(\mathbf{x}) d\Omega = -\int_\Omega c \nabla u(\mathbf{x}) \nabla v(\mathbf{x}) d\Omega + \int_{\delta\Omega} v(\mathbf{x}) c \frac{\partial u}{\partial n} d\Gamma$, where $\delta\Omega$ is the boundary of the domain Ω, and $\vec{n}$ is the outward normal to the boundary.

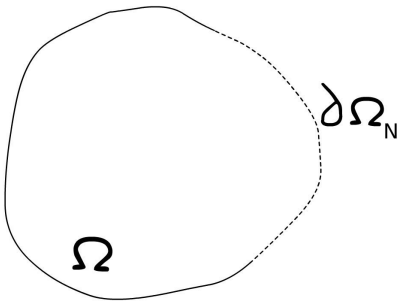

Figure 4.1: The domain Ω, with the boundary $\delta\Omega$, which include a traction boundary $\delta\Omega_N$.

we obtain these system of equations for a and b,

$$\sum_{j}^{nnod} a_j^l \int_\Omega N_i N_j (1 + \Delta t k w(\mathbf{x})^l) d\Omega = \sum_{j}^{nnod} a_j^{l-1} \int_\Omega N_i N_j d\Omega \,, \tag{4.16}$$

$$\sum_{j}^{nnod} b_j^l \int_\Omega N_i N_j d\Omega = \sum_{j}^{nnod} b_j^{l-1} \int_\Omega N_i N_j d\Omega - \Delta t k \int_\Omega N_i w(\mathbf{x})^l a(\mathbf{x})^l d\Omega \,, \tag{4.17}$$

for $i = 1, 2, ..., \text{nnod}$.

For the linear system of equations in Eqs. 4.15, 4.16 and 4.17, each element is mapped onto a reference element and then the integration is performed with the Gaussian integration point loop, before they are assembled onto the global matrix again. Then the full linear system of equations can be solved when a sparse storage is used, and we solve with the help of Matlab's *backslash*-operator.

The mechanical solver is taking the concentration b as an input to calculate the stress built up by the volume changes due to the reaction, where the eigenstrain term is given by,

$$\epsilon^* = \beta \frac{b(\mathbf{x})}{b_0}$$

The discretization of the mechanical model follows.

4.2.2 Mechanical model

The equations to be solved for the mechanical problem are from the boundary value problem given in Chapter 2; the force equilibrium condition and a traction boundary condition,

$$\sigma_{ij,j} + f_i = 0 \quad \text{in} \quad \Omega \tag{4.18}$$

$$\sigma_{ij} n_j = h_i \quad \text{in} \quad \delta\Omega_N \tag{4.19}$$

The domain is shown in Figure 4.1.

First we multiply the residual in Eq.4.18 with a weighting function N, and then integrate over the domain.

$$\int_\Omega N_i(\sigma_{ij,j} + f_i)d\Omega = 0$$
$$\int_\Omega N_i\sigma_{ij,j}d\Omega = -\int_\Omega w_i f_i d\Omega$$

where the index i now is the cartesian directions $i = x, y$, and the same for j.

Performing integration by parts, and the weak formulation of the Galerkin FEM becomes,

$$\int_\Omega w_i\sigma_{ij,j}d\Omega = \int_{\delta\Omega} w_i\sigma_{ij}n_j d\Gamma - \int_\Omega w_{i,j}\sigma_{ij}d\Omega \; . \tag{4.20}$$

where Green's lemma is used, and $d\Gamma$ is the curve integral over the boundary $\delta\Omega$. From the traction boundary condition in Eq. 4.19 we recognize that the term $\sigma_{ij}n_j = h_i$, and Eq. 4.20 becomes,

$$\int_\Omega w_{(i,j)}\sigma_{ij}d\Omega = \int_\Omega w_i f_i d\Omega + \int_{\delta\Omega} w_i h_i d\Gamma \tag{4.21}$$

The stress is related to the strain through the relation,

$$\sigma_{ij} = \lambda(\epsilon_{kk} - \epsilon^*)\delta_{ij} + 2\mu\epsilon_{ij} \tag{4.22}$$

where λ and μ denotes the Lamé's parameters, and the δ_{ij} is the Kronecker delta.

In our two-dimensional code we assume a plain strain condition, $\epsilon_{zz} = \epsilon_{xz} = \epsilon_{yz} = 0$, this does not mean that $\sigma_{zz} = 0$. Writing the stress-strain relation in Eq. 4.22 using Voigt notation[2] gives,

$$\begin{pmatrix} \sigma_{xx} \\ \sigma_{yy} \\ \sigma_{zz} \\ \sigma_{xy} \end{pmatrix} = \begin{pmatrix} \lambda+2\mu & \lambda & \lambda & 0 \\ \lambda & \lambda+2\mu & \lambda & 0 \\ \lambda & \lambda & \lambda+2\mu & 0 \\ 0 & 0 & 0 & \mu \end{pmatrix} \left(\begin{pmatrix} \gamma_{xx} \\ \gamma_{yy} \\ 0 \\ \gamma_{xy} \end{pmatrix} - \begin{pmatrix} \epsilon^* \\ \epsilon^* \\ \epsilon^* \\ 0 \end{pmatrix} \right) ,$$

where we denote the matrix, $\mathbf{D}_L$. The vector γ is the engineering strain vector with the components, $\gamma_{xx} = \epsilon_{xx}$, $\gamma_{yy} = \epsilon_{yy}$ and $\gamma_{xy} = 2\epsilon_{xy}$.

The relation between the engineering strain and the displacement in Voigt-notation is,

$$\begin{pmatrix} \epsilon_{xx} \\ \epsilon_{yy} \\ 2\epsilon_{xy} \end{pmatrix} = \begin{pmatrix} \frac{\partial u_x}{\partial x} \\ \frac{\partial u_y}{\partial y} \\ \frac{\partial u_x}{\partial y} + \frac{\partial u_y}{\partial x} \end{pmatrix}$$

The two components, i.e. x and y, of the displacement field are approximated using a linear combination of shape functions

$$u(\mathbf{x}) \approx \hat{u}(\mathbf{x}) = \sum_j^{nnod} u_j N_j(\mathbf{x})$$

[2]Voigt notation is a way to represent a symmetric tensor, with pseudo-vectors.

where *nnod* is the number of nodes in the computational domain, and N_j are the shape functions.

For first order triangular elements, i.e. with three nodes, we introduce the storage convention for the degrees of freedom of displacement in each element,

$$\vec{u} = \left(u_x^1, u_y^1, u_x^2, u_y^2, u_x^3, u_y^3\right)^T .$$

In Voigt notation the relation between the total strain and the approximated displacement becomes,

$$\begin{pmatrix} \gamma_{xx} \\ \gamma_{yy} \\ \gamma_{xy} \end{pmatrix} = \begin{pmatrix} \frac{\partial N_1}{\partial x} & 0 & \frac{\partial N_2}{\partial x} & 0 & \frac{\partial N_3}{\partial x} & 0 \\ 0 & \frac{\partial N_1}{\partial y} & 0 & \frac{\partial N_2}{\partial y} & 0 & \frac{\partial N_3}{\partial y} \\ \frac{\partial N_1}{\partial y} & \frac{\partial N_1}{\partial x} & \frac{\partial N_2}{\partial y} & \frac{\partial N_2}{\partial x} & \frac{\partial N_3}{\partial y} & \frac{\partial N_3}{\partial x} \end{pmatrix} \begin{pmatrix} u_x^1 \\ u_y^1 \\ u_x^2 \\ u_y^2 \\ u_x^3 \\ u_y^3 \end{pmatrix}$$

or $\gamma = Bu$ in vector notation. The stress - strain relation is then inserted,

$$\sigma = D(\gamma - \epsilon^*) = D\left(B\mathbf{u} - \epsilon^*\right) .$$

From the stress equilibrium in Eq. 4.21, we can now insert for the above equations, and in the end get the linear system of equations,

$$\mathbf{u} \int_\Omega B^T D B d\Omega = \int_\Omega B^T f d\Omega + \int_{\delta\Omega_N} B^T h d\Gamma - \int_\Omega B^T D \delta\epsilon^* d\Omega , \tag{4.23}$$

where the right hand side is known, and we want to find the displacement u. The part with the eigenstrain is solved before solving for the displacement, and is hence moved to the right-hand side of the equation. The system of equations can now be solved in the same manner as described in the previous section.

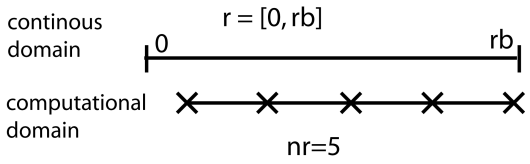

Figure 4.2: The discretized domain in polar coordinates, without solving for the center node. Starting instead at $\Delta r/2$.

4.3 The coupled transient reaction-diffusion and mechanical problem in polar coordinates

To study the problem on different geometries a FDM-code is developed in polar coordinates.

Assuming a plain strain condition for the vertical direction, a homogeneous cylinder, and axisymmetric boundary and initial conditions, leaves us with only variations in the radial direction.

When axisymmetric problems are modeled, one often need a condition for the center coordinate $r = 0$, because one often end up dividing by zero. We choose to use the approach discussed briefly in Lai et al. (2007), where the domain, $r \in [0, r_b]$, is discretization so that we do not solve for the center coordinate,

$$r_i = (i - 1/2)\Delta r \text{ , where } \Delta r = 2r_b/(2n_r - 1) \text{ , and } i = 1, 2, ..., n_r \text{ .}$$

This gives us with a domain starting $r_1 = 1/2\Delta r$ from the center, and goes to $r_{n_r} = r_b$. The discretized domain is shown in Figure 4.2 for a case with just $n_r = 5$ for illustration purposes.

4.3.1 Reaction-diffusion problem

In polar coordinates the axisymmetric reaction-diffusion problem yields,

$$\frac{\partial w}{\partial t} = D\frac{1}{r}\frac{\partial}{\partial r}\left(r\frac{\partial w}{\partial r}\right) - \rho Q \tag{4.24}$$

where the stoichiometric constant used in the previous sections now is defined as $r_{\text{stoichiometric}} = \rho$, to avoid troubles with the r denoting the radial coordinate. The boundary condition is $w(r_b, t) = w_0$, with an initial condition $w(r, 1) = 0$ for $r \in [0, r_b)$.

The evolution of the other concentrations, a and b, is the same as for the 1D-model, but with a radial dependence $a(r)$ and $b(r)$.

The FDM discretization of the concentration is, $w(r, t) = w(i\Delta r, t_0 + l\Delta t)$. An implicit scheme for the temporal derivative is introduced,

$$\frac{w_i^{l+1} - w_i^l}{\Delta t} = D\frac{1}{r_i}\frac{\partial}{\partial r}\left(r_i\frac{\partial w_i^{l+1}}{\partial r}\right) - \rho k w_i^{l+1} a_i^l$$

For the spatial derivative, we use a centered difference scheme,

$$w_i^{l+1} - \Delta t \frac{D}{r_i}\left(\frac{w_{i-1}^{l+1}(r_{i-1/2}) - w_i^{l+1}(r_{i+1/2} + r_{i-1/2}) + w_{i+1}^{l+1}(r_{i+1/2})}{\Delta r^2}\right) + \Delta t \rho w_i^{l+1} a_i^l = w_i^l \, .$$

Multiply with r_i and rearrange to a simpler form,

$$w_{i-1}^{l+1}\big(-D\frac{\Delta t}{\Delta r^2} r_{i-11/2}\big) + w_i^{l+1}\big(r_i + D\frac{\Delta t}{\Delta r^2}(r_{i+1/2} + r_{i-1/2}) + \Delta t \rho k a_i^l r_i\big) + w_{i+1}^{l+1}\big(-D\frac{\Delta t}{\Delta r^2} r_{i+1/2}\big) = w_i^l r_i \, . \tag{4.25}$$

This system can be written into a system of linear equations,

$$H w^{l+1} = w^l r$$

where H is a matrix with the coefficients of w_i^{l+1} on the diagonal and the coefficients of w_{i-1}^{l+1} and w_{i+1}^{l+1} on the -1 and +1 off-diagonal, respectively.

The concentration of W is then used to solve for the concentration of A, and in turn the concentration of B, which produces the strain,

$$\epsilon^* = \beta \frac{b(r)}{b_0}$$

To fully solve the mechanical problem, we also need the stress-strain relations, and equilibrium condition, in polar coordinates.

4.3.2 Mechanical problem

The equilibrium condition for the stresses in cylindrical polar coordinates are (Fung (1965)),

$$\begin{aligned} \frac{1}{r}\frac{\partial}{\partial r}(r\sigma_r) + \frac{1}{r}\frac{\partial}{\partial \theta}(\sigma_{r\theta}) + \frac{\partial}{\partial z}(\sigma_{rz}) - \frac{\sigma_\theta}{r} &= -F_r \, , \\ \frac{1}{r^2}\frac{\partial}{\partial r}(r^2\sigma_{\theta r}) + \frac{1}{r}\frac{\partial}{\partial \theta}(\sigma_\theta) + \frac{\partial}{\partial z}(\sigma_{\theta z}) &= -F_\theta \, , \\ \frac{1}{r}\frac{\partial}{\partial r}(r\sigma_{zr}) + \frac{1}{r}\frac{\partial}{\partial \theta}(\sigma_{z\theta}) + \frac{\partial}{\partial z}(\sigma_z) &= -F_z \, . \end{aligned}$$

In our problem no body forces are present, $\vec{F} = 0$, and if no variations in z- or θ-directions are assumed, the equilibrium condition becomes,

$$\frac{\partial \sigma_r}{\partial r} + \frac{\sigma_r - \sigma_\theta}{r} = 0 \, . \tag{4.26}$$

Like for the two-dimensional case in Section 4.2.2, a plain strain assumption is made, $\epsilon_z = 0 = \epsilon_{rz} = \epsilon_{\theta z}$. The stress-strain relations in polar coordinates yields

then,

$$\sigma_r = \frac{E}{(1+\nu)(1-2\nu)}\Big[(1-\nu)\epsilon_r + \nu\epsilon_\theta - \epsilon^*(1+\nu)\Big] ,$$
$$\sigma_\theta = \frac{E}{(1+\nu)(1-2\nu)}\Big[\nu\epsilon_r + (1-\nu)\epsilon_\theta - \epsilon^*(1+\nu)\Big] ,$$
$$\sigma_z = \nu(\sigma_r + \sigma_\theta) - \epsilon^* E .$$

The elastic strains are related to the displacement in the following way,

$$\epsilon_r = \frac{\partial u_r}{\partial r}$$
$$\epsilon_\theta = \frac{1}{r}\frac{\partial u_\theta}{\partial \theta} + \frac{u_r}{r} = \frac{u_r}{r}$$

After inserting the relations for displacement in Eq. 4.26, we get

$$\frac{\partial^2 u}{\partial r^2} + \frac{1}{r}\frac{\partial u}{\partial r} - \frac{1}{r^2}u = \frac{1+\nu}{1-\nu}\frac{\partial \epsilon^*}{\partial r}$$

This PDE is now discretized using the finite difference method, and a centred difference scheme is used on the derivatives,

$$\frac{u_{i+1} - 2u_i + u_{i-1}}{\Delta r^2} + \frac{1}{r_i}\frac{u_{i+1} - u_{i-1}}{2\Delta r} - \frac{1}{r_i^2}u_i = \frac{1+\nu}{1-\nu}\frac{\partial \epsilon_i^*}{\partial r} ,$$

the right hand side is known from the reaction-diffusion part, and the derivative of the eigenstrain is not discretized to emphasize that. Rearrange into the different displacement indexes,

$$u_{i-1}\Big(\frac{2r_i - \Delta r}{2\Delta r^2\, r_i}\Big) + u_i\Big(\frac{-2r_i^2 - \Delta r^2}{\Delta r^2\, r_i^2}\Big) + u_{i+1}\Big(\frac{2r_i + \Delta r}{2\Delta r^2\, r_i}\Big) = \frac{1+\nu}{1-\nu}\frac{\partial \epsilon_i^*}{\partial r}$$

To get a symmetric matrix in the end, we multiply with $2\Delta r^2 r_i$

$$u_{i-1}\Big(2r_i - \Delta r\Big) + u_i\Big(\frac{-4r_i^2 - 2\Delta r^2}{r_i}\Big) + u_{i+1}\Big(2r_i + \Delta r\Big) = \frac{1+\nu}{1-\nu}\frac{\partial \epsilon_i^*}{\partial r} 2\Delta r^2\, r_i . \quad (4.27)$$

We have now a linear system of equations on the form,

$$Hu = g ,$$

where H is the matrix with the coefficients of u, and the vector g is $g = \frac{1+\nu}{1-\nu}\frac{\partial \epsilon_i^*}{\partial r} 2\Delta r^2\, r_i$.

Chapter 5

Benchmarking

After developing a numerical model it is important to check if the model gives appropriate results, and benchmark the code. That is, to test the model on a problem you know that you have the correct answer to. The best way to benchmark a model is, if possible, to check with an analytical solution to the problem.

In this chapter an analytical solution for thermally induced stresses in a cylinder will be derived, together with a solution for thermal diffusion in a cylinder. In the last section of this chapter the analytical solutions will be tested with the numerical models, both the two-dimensional finite element code, by using a circular domain, and the cylindrical finite difference code.

5.1 Derivation of the analytical solution

The analytical derivations of the problem with thermally induced stress in a cylinder, will be divided into three parts. First the mechanical equations will be derived, then thermal diffusion, and finally the two will be coupled. The derivations will follow the derivations done by Timoshenko and Goodier (1970) on the same problem, with some additional steps in between.

5.1.1 Stress in a cylinder

The stress tensor for an element in a cylinder is,

$$\sigma_{cylinder} = \begin{pmatrix} \sigma_{rr} & \sigma_{r\theta} & \sigma_{rz} \\ \sigma_{\theta r} & \sigma_{\theta\theta} & \sigma_{\theta z} \\ \sigma_{zr} & \sigma_{z\theta} & \sigma_{zz} \end{pmatrix},$$

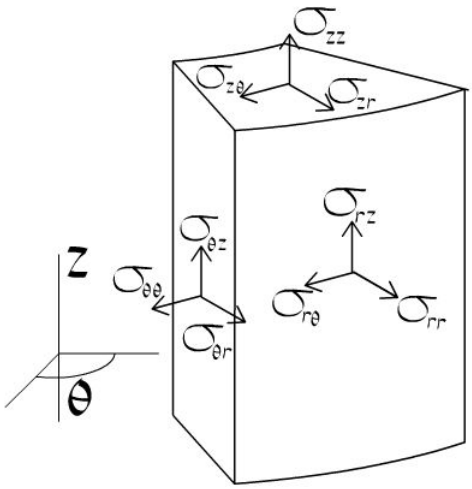

Figure 5.1: Stresses on a cylindrical element.

and the setup is shown in figure 5.1. The equilibrium condition that must be fulfilled for each element in the cylinder is (Fung (1965)),

$$\begin{aligned}
\frac{1}{r}\frac{\partial}{\partial r}(r\sigma_r) + \frac{1}{r}\frac{\partial}{\partial \theta}(\sigma_{r\theta}) + \frac{\partial}{\partial z}(\sigma_{rz}) - \frac{\sigma_\theta}{r} &= -F_r \ , \\
\frac{1}{r^2}\frac{\partial}{\partial r}(r^2\sigma_{\theta r}) + \frac{1}{r}\frac{\partial}{\partial \theta}(\sigma_\theta) + \frac{\partial}{\partial z}(\sigma_{\theta z}) &= -F_\theta \ , \\
\frac{1}{r}\frac{\partial}{\partial r}(r\sigma_{zr}) + \frac{1}{r}\frac{\partial}{\partial \theta}(\sigma_{z\theta}) + \frac{\partial}{\partial z}(\sigma_z) &= -F_z \ .
\end{aligned}$$

The components off-diagonal in the stress tensor are assumed to be equal (otherwise the element would be subject for unconstrained rotation), thus $\sigma_{r\theta} = \sigma_{\theta r}$, $\sigma_{rz} = \sigma_{zr}$, and $\sigma_{\theta z} = \sigma_{z\theta}$. In the symmetrical case all the shear components will cancel out, and we have $\sigma_{r\theta} = 0$, $\sigma_{rz} = 0$, and $\sigma_{\theta z} = 0$. For simplification of notation the remaining non-zero stresses are set to σ_r, σ_θ and σ_z.

For a long circular cylinder the temperature is assumed to be symmetrical about the axis and independent of the axial-coordinate z. The axial displacement, ω, is also assumed to be zero.

The stress-strain relations in polar coordinates are,

$$\begin{aligned}
\epsilon_r - \alpha T &= \frac{1}{E}\Big[\sigma_r - \nu(\sigma_\theta + \sigma_z)\Big] \ , \\
\epsilon_\theta - \alpha T &= \frac{1}{E}\Big[\sigma_\theta - \nu(\sigma_r + \sigma_z)\Big] \ , \\
\epsilon_z - \alpha T &= \frac{1}{E}\Big[\sigma_z - \nu(\sigma_r + \sigma_\theta)\Big] \ .
\end{aligned}$$

with α begin the thermal stress coefficient, and are assumed constant throughout the sphere, E Youngs modulus, ν Poissons ratio, and ϵ the elastic strain. Since the axial displacement is assumed to be zero ($\omega = 0$), it means that a plain strain

assumption is done, and that ϵ_z also equals zero, and we get this expression for the axial-component of stress,

$$\sigma_z = \nu(\sigma_r + \sigma_\theta) - \alpha E T \,. \tag{5.1}$$

Inserting this into the other stress-strain relations gives,

$$\begin{aligned} \epsilon_r - \alpha T &= \frac{1}{E}\Big[\sigma_r - \nu\sigma_\theta - \nu^2\sigma_r - \nu^2\sigma_\theta + \nu\alpha E T\Big] \,, \\ &= \frac{1}{E}\Big[\sigma_r(1-\nu^2) - \nu\sigma_\theta(1+\nu) + \nu\alpha E T\Big] \,, \\ \implies \epsilon_r - \alpha T(1+\nu) &= \frac{1+\nu}{E}\Big[\sigma_r(1-\nu) - \nu\sigma_\theta\Big] \,. \end{aligned}$$

And similar for θ,

$$\epsilon_\theta - \alpha T(1+\nu) = \frac{1+\nu}{E}\Big[\sigma_\theta(1-\nu) - \nu\sigma_r\Big] \,.$$

It is now possible to derive expressions for the stresses,

$$\begin{aligned} \sigma_r &= \frac{E}{1+\nu}\frac{1}{1-\nu}\big(\epsilon_r - \alpha T(1+\nu)\big) + \frac{\nu\sigma_\theta}{1-\nu} \,, \\ \sigma_\theta &= \frac{E}{1+\nu}\frac{1}{1-\nu}\big(\epsilon_\theta - \alpha T(1+\nu)\big) + \frac{\nu\sigma_r}{1-\nu} \,. \end{aligned}$$

Inserting the two equations above into each other will give,

$$\begin{aligned} \sigma_r &= \frac{E}{(1+\nu)(1-2\nu)}\Big[(1-\nu)\epsilon_r + \nu\epsilon_\theta - \alpha T(1+\nu)\Big] \,, \\ \sigma_\theta &= \frac{E}{(1+\nu)(1-2\nu)}\Big[(1-\nu)\epsilon_\theta + \nu\epsilon_r - \alpha T(1+\nu)\Big] \,. \end{aligned}$$

The radial displacement in the cylinder, u, has these relations to the elastic strain,

$$\epsilon_r = \frac{du}{dr} \quad \epsilon_\theta = \frac{u}{r} \,. \tag{5.2}$$

Substituting the relations between strain and displacement (eq.5.2) gives,

$$\sigma_r = \frac{E}{(1+\nu)(1-2\nu)}\Big[(1-\nu)\frac{du}{dr} + \nu\frac{u}{r} - \alpha T(1+\nu)\Big] \,, \tag{5.3}$$

$$\sigma_\theta = \frac{E}{(1+\nu)(1-2\nu)}\Big[\nu\frac{du}{dr} + (1-\nu)\frac{u}{r} - \alpha T(1+\nu)\Big] \,. \tag{5.4}$$

Expressions for the stresses in a cylinder are now found in equations 5.1, 5.3 and 5.4. These must fulfill the equilibrium condition for stresses. With no variations in z and θ the equilibrium condition for the stresses becomes,

$$\frac{d\sigma_r}{dr} + \frac{\sigma_r - \sigma_\theta}{r} = 0 \,.$$

Inserting the above found expressions for stresses into this equilibrium condition, will give us a partial differential equation for the displacement u,

$$\Big[(1-\nu)\frac{d^2u}{dr^2}+\nu\frac{d}{dr}(\frac{u}{r})-\alpha(1+\nu)\frac{dT}{dr}\Big]+ \frac{(1-\nu)du/dr-\nu dr/dr+\nu u/r-(1-\nu)u/r}{r}=0\,,$$

$$\implies (1-\nu)\frac{d^2u}{dr^2}+\frac{(1-\nu)}{r}\frac{du}{dr}-\frac{(1-\nu)}{r^2}u=\alpha(1+\nu)\frac{dT}{dr}\,,$$

$$\implies \frac{d^2u}{dr^2}+\frac{1}{r}\frac{du}{dr}-\frac{1}{r^2}u=\alpha\frac{(1+\nu)}{(1-\nu)}\frac{dT}{dr}\,. \tag{5.5}$$

This inhomogeneous second order differential equation (Eq.5.5), can be solved in order to obtain an expression for the displacement u.

Starting out with the homogeneous equations, that is setting the right hand side equal to zero, we have,

$$u''+\frac{1}{r}u'-\frac{1}{r^2}u=0 \tag{5.6}$$

If $u_1(r)$ and $u_2(r)$ both are a solution of the equation, then also $u(r)=c_1u_1(r)+c_2u_2(r)$ is a solution if $u_1(r)$ and $u_2(r)$ are linearly independent, and c_1 and c_2 are constants.

By substitution we can see that $u_1(r)=r$ must be a solution to the equation. Another solution can be found by inserting, $u_2(r)=C(r)u_1(r)=C(r)r$, into the homogeneous equation.

$$\begin{aligned}
&\big(C(r)r\big)''+\frac{1}{r}\big(C(r)r\big)'-\frac{1}{r^2}C(r)r=0\\
&C''(r)r+2C'(r)+\frac{1}{r}C'(r)r+\frac{1}{r}C(r)-\frac{1}{r}C(r)=0\\
&C''(r)r+3C'(r)=0\\
&\frac{dC'(r)}{dr}=-\frac{3}{r}C'(r)\\
&\frac{dC'(r)}{C'(r)}=-\frac{3}{r}dr\\
&\int\frac{1}{C'(r)}dC'(r)=-3\int\frac{1}{r}dr\\
&\ln C'(r)=-3(\ln r+A)\\
&C'(r)=Ar^{-3}\\
&C(r)=A\int\frac{1}{r^3}dr=-\frac{A}{2r^2}+B\,,
\end{aligned}$$

where A and B are integration constants. Recall the second solution $u_2=C(r)u_1=C(r)r$. The two solutions are linearly independent regardless of the constants A and B. The constants are therefor chosen to be $A=-2$ and $B=0$ for simplicity. This makes $u_2=\frac{1}{r}$, and gives the solution to the homogeneous equation, Eq.5.6,

$$u_h(r)=C_1r+C_2\frac{1}{r}\,.$$

To solve the inhomogeneous part of the PDE (Eq.5.5), the left-hand-side is rewritten like,

$$\frac{d^2u}{dr^2} + \frac{1}{r}\frac{du}{dr} - \frac{1}{r^2}u = \frac{d}{dr}\left[\frac{1}{2r^2}\frac{d}{dr}(r^2u) + \frac{1}{2}\frac{du}{dr}\right] ,$$

so that the equation looks like,

$$\frac{d}{dr}\left[\frac{1}{2r^2}\frac{d}{dr}(r^2u) + \frac{1}{2}\frac{du}{dr}\right] = \frac{(1+\nu)}{(1-\nu)}\alpha\frac{dT}{dr} . \tag{5.7}$$

If we perform integration over r on both sides, we get,

$$\begin{aligned}
\int \frac{d}{dr}\left[\frac{1}{2r^2}\frac{d}{dr}(r^2u) + \frac{1}{2}\frac{du}{dr}\right] dr &= \int \frac{(1+\nu)}{(1-\nu)}\alpha\frac{dT}{dr}dr , \\
\frac{1}{2r^2}\frac{d}{dr}(r^2u) + \frac{1}{2}\frac{du}{dr} &= \frac{(1+\nu)}{(1-\nu)}\alpha T , \\
\frac{1}{2r^2}\left(r^2\frac{du}{dr} + 2ru\right) + \frac{1}{2}\frac{du}{dr} &= \frac{(1+\nu)}{(1-\nu)}\alpha T , \\
\frac{du}{dr} + \frac{1}{r}u &= \frac{(1+\nu)}{(1-\nu)}\alpha T .
\end{aligned}$$

This is now a linear first-order equation on the form, $y' + P(x)y = Q(x)$, which can be solved by using the formula,

$$y(x) = e^{-I}\int Q(x)e^I dx + ce^{-I} ,$$

where $I = \int P dx$ and c is an integration constant.

Let us first take the integral, I, from the term in front of u,

$$\begin{aligned}
I &= \int \frac{1}{r}dr = \ln(r) \\
e^I &= e^{\ln(r)} = r \\
\implies u &= \frac{1}{r}\int_a^r \frac{(1+\nu)}{(1-\nu)}\alpha T r dr .
\end{aligned}$$

The constant c-term from the formula would give rise to the homogeneous solution already found above. The integral is taken over the radius r of the sphere. The particular solution to Eq.5.5 becomes then,

$$u_p(r) = \frac{1+\nu}{1-\nu}\alpha\frac{1}{r}\int_a^r Tr\, dr .$$

The complete solution to the inhomogeneous differential equation Eq.5.5 is then the homogeneous solution plus the particular solution,

$$\begin{aligned}
u &= u_h(r) + u_p(r) , \\
u &= \frac{1+\nu}{1-\nu}\alpha\frac{1}{r}\int_a^r Tr dr + C_1 r + \frac{C_2}{r} .
\end{aligned} \tag{5.8}$$

The solution for the displacement is now found, and can be solved if the temperature is known. In the end it is the stresses that we want to solve for an therefor we insert this relation into the previous found relations for the strain, and finally the stress. From the relations between strain and displacement in eq.5.2, and the equation of u, eq.5.8, new expressions for the stresses can be derived,

$$\sigma_r = -\frac{\alpha E}{1-\nu}\frac{1}{r^2}\int_a^r Trdr + \frac{E}{1+\nu}\left(\frac{C_1}{1-2\nu} - \frac{C_2}{r^2}\right) , \tag{5.9}$$

$$\sigma_\theta = \frac{\alpha E}{1-\nu}\frac{1}{r^2}\int_a^r Trdr - \frac{\alpha E T}{1-\nu} + \frac{E}{1+\nu}\left(\frac{C_1}{1-2\nu} + \frac{C_2}{r^2}\right) , \tag{5.10}$$

and for the stress in axial direction, we get from eq.5.1 that,

$$\sigma_z = -\frac{\alpha E T}{1-\nu} + \frac{2\nu E C_1}{(1+\nu)(1-2\nu)} . \tag{5.11}$$

Since we have made the assumption that $\omega = 0$, a normal force distributed at the ends of the cylinder must equal eq.5.11, in order to make the forces balance. This can also be done with superposing a uniform axial stress $\sigma_z = C_3$, if C_3 is so that the resultant force on the ends is zero.

We will then get an extra term in the equation for the displacement eq.5.8, $-\nu C_3 r/E$, on the right side. The stresses σ_r and σ_θ will still be the same as in eq.5.9 and eq.5.10, respectively.

For a solid cylinder the lower limit in the integrals a is set to zero. The integration constants C_1, C_2 and C_3, must be determined from the boundary conditions of the problem.

In a uniform cylinder, with symmetric temperature distribution, the radial displacement, u, at the center $r = 0$ must be equal to zero. From eq.5.8 we see that $C_2 = 0$ fulfill this condition.

Similar as for the sphere, we must restrain the normal stress at the surface $r = b$, thus setting σ_r equal zero at $r = b$ gives the expression for C_1,

$$\begin{aligned} 0 &= -\frac{\alpha E}{1-\nu}\frac{1}{b^2}\int_0^b Trdr + \frac{E}{1+\nu}\frac{C_1}{1-2\nu} \\ \Longrightarrow \frac{C_1}{(1+\nu)(1-2\nu)} &= -\frac{\alpha}{1-\nu}\frac{1}{b^2}\int_0^b Trdr \end{aligned}$$

From the axial stress in eq.5.11 we can find the resultant force at the ends,

$$\int_0^b \sigma_z 2\pi r dr = -\frac{\alpha E}{1-\nu}\int_0^b 2\pi r T dr + \frac{2\nu E C_1}{(1+\nu)(1-2\nu)}\pi b^2 ,$$

The superimposed uniform axial stress C_3, has the resultant $C_3\pi b^2$. To make the total axial force zero these two must be set equal, thus,

$$C_3\pi b^2 = \frac{\alpha E}{1-\nu}\int_0^b 2\pi r T dr - \frac{2\nu E C_1}{(1+\nu)(1-2\nu)}\pi b^2 . \tag{5.12}$$

All the constants are now found, and we can insert for the constants in eq.5.8, 5.9, 5.10 and 5.11,

$$u = \frac{1+\nu}{1-\nu}\alpha\left((1-2\nu)\frac{r}{b^2}\int_0^b Trdr + \frac{1}{r}\int_0^r Trdr\right), \tag{5.13}$$

$$\sigma_r = \frac{\alpha E}{1-\nu}\left(\frac{1}{b^2}\int_0^b Trdr - \frac{1}{r^2}\int_0^r Trdr\right), \tag{5.14}$$

$$\sigma_\theta = \frac{\alpha E}{1-\nu}\left(\frac{1}{b^2}\int_0^b Trdr + \frac{1}{r^2}\int_0^r Trdr - T\right), \tag{5.15}$$

$$\sigma_z = \frac{\alpha E}{1-\nu}\left(\frac{2\nu}{b^2}\int_0^b Trdr - T\right). \tag{5.16}$$

These equations holds for the case of zero axial strain ($\epsilon_z = 0$), as assumed in the derivations.

If we want to study the case with zero axial force ($F_z = 0$), σ_r and σ_θ will be the same, but for u and σ_z the new expressions becomes,

$$u = \frac{1+\nu}{1-\nu}\alpha\left(\frac{1-3\nu}{1+\nu}\frac{r}{b^2}\int_0^b Trdr + \frac{1}{r}\int_0^r Trdr\right), \tag{5.17}$$

$$\sigma_z = \frac{\alpha E}{1-\nu}\left(\frac{2}{b^2}\int_0^b Trdr - T\right). \tag{5.18}$$

To make use of these expressions for the stresses we now need to know the temperature distribution in the cylinder.

5.1.2 Thermal diffusion in cylinder

Diffusion of heat in an isotropic medium is given by the diffusion equation,

$$\frac{\partial T}{\partial t} = \frac{k}{c_p \rho} \nabla^2 T \,, \tag{5.19}$$

where k is the thermal conductivity , c_p is the specific heat capacity, and ρ is the density. All together this is called the thermal diffusivity, and is denoted by,

$$\kappa = \frac{k}{c_p \rho} \,.$$

In cylindrical coordinates the diffusion equations yields,

$$\frac{\partial T(r,\theta,z,t)}{\partial t} = \kappa \left(\frac{1}{r} \frac{\partial}{\partial r} \left(r \frac{\partial T}{\partial r} \right) + \frac{1}{r^2} \frac{\partial^2 T}{\partial \theta^2} + \frac{\partial^2 T}{\partial z^2} \right) \,. \tag{5.20}$$

In the above calculations of stress we have assumed axial symmetry of temperature, and we will here study a two-dimensional problem, thus the temperature is only depending on r. Therefore we can skip the two last terms in eq.5.20.

In order to solve this differential equation for T, the technique of separation of variables is used,

$$T(r,t) = G(r)H(t) \,.$$

This gives the diffusion equation,

$$\begin{aligned} G(r) \frac{\partial H(t)}{\partial t} &= \kappa \left(H(t) \frac{1}{r} \frac{\partial}{\partial r} \left(r \frac{\partial G(r)}{\partial r} \right) \right) \,, \\ \implies \frac{1}{H(t)} \frac{dH(t)}{dt} &= \kappa \frac{1}{G(r)} \frac{1}{r} \frac{d}{dr} \left(r \frac{dG(r)}{dr} \right) = -C \,, \end{aligned} \tag{5.21}$$

where C is a constant. The time dependent equation gives,

$$\begin{aligned} \frac{dH(t)}{dt} &= -CH(t) \,, \\ \implies H(t) &= d_1 e^{-Ct} \,, \end{aligned} \tag{5.22}$$

where d_1 is a constant.

The equation with the radial dependence gives,

$$\begin{aligned} &\kappa \frac{1}{r} \frac{d}{dr} \left(r \frac{dG(r)}{dr} \right) + G(r)C = 0 \,, \\ &\kappa \frac{d^2 G(r)}{dr^2} + \kappa \frac{1}{r} \frac{dG(r)}{dr} + G(r)C = 0 \,, \\ &\kappa r^2 \frac{d^2 G(r)}{dr^2} + \kappa r \frac{dG(r)}{dr} + r^2 G(r)C = 0 \,, \\ &r^2 \frac{d^2 G(r)}{dr^2} + r \frac{dG(r)}{dr} + \frac{C}{\kappa} r^2 G(r) = 0 \,, \end{aligned} \tag{5.23}$$

which can be recognized as the Bessel differential equation[1], with an additional constant in front of the last term. The solution to this equation is

$$G(r) = d_2 J_0\left(\sqrt{\frac{C}{\kappa}}r\right) + d_3 Y_0\left(\sqrt{\frac{C}{\kappa}}r\right) , \tag{5.24}$$

where J_0 is the first order Bessel function[2], Y_0 is the second order Bessel function, and d_2, d_3 are constants. The second order Bessel function $Y_0(x)$ is divergent at $x = 0$. Since it is no infinite source or sink at $r = 0$ in our problem, the constant d_3 must be set to zero.

From eq.5.22 and 5.24 the expression for the temperature becomes,

$$T(r,t) = H(t)G(r) = d\, e^{-Ct} J_0\left(\sqrt{\frac{C}{\kappa}}r\right) , \tag{5.25}$$

where the constant $d = d_1 d_2$. To be able to determine the constants, boundary conditions must be addressed. The temperature at the rim of the cylinder is set equal to zero, $T(r = 1, t) = 0$,

$$\begin{aligned} T(1,t) &= de^{-Ct} J_0\left(\sqrt{\frac{C}{\kappa}}b\right) = 0 , \\ \Longrightarrow \sqrt{\frac{C}{\kappa}}b &= \beta_n , \end{aligned}$$

where β_n is the roots of J_0. The constant C is thus: $C_n = \beta_n^2 \kappa / b^2$. Eq.5.25 then becomes,

$$T(r,t) = \sum_{n=1}^{\infty} d J_0\big(\beta_n \frac{r}{b}\big) e^{-\beta_n^2 \kappa t} . \tag{5.26}$$

Due to symmetry there should be no change in T over $r = 0$,

$$\left.\frac{\partial T}{\partial r}\right|_{r=0} = -\sum_{n=1}^{\infty} d\beta_n J_1\big(0\big) e^{-\beta_n^2 \kappa t} = 0 ,$$

this holds, because $J_1(0) = 0$.

The initial temperature distribution is set at $T(r, 0) = T_0$ for $r \in [0, r)$,

$$T(r,0) = \sum_{n=1}^{\infty} d J_0(\beta_n \frac{r}{b}) = T_0 . \tag{5.27}$$

To be able to solve this equation for d we must make use of the orthogonality of the Bessel functions. For two first order Bessel functions of the same number, we have the orthogonality relation,

$$\int_0^1 x J_p(\beta_m x) J_p(\beta_n x) dx = \frac{\delta_{mn}}{2} \big[J_{p+1}(\beta_m)\big]^2 ,$$

[1] The Bessel function: $x^2\xi''(x) + x\xi'(x) + x^2\xi(x) = 0$, has the solution $\xi(x) = d_1 J_0(x) + d_2 Y_0(x)$.

[2] $J_k(x) = \sum_{n=1}^{\infty} \frac{(-1)^n (x/2)^{k+2n}}{n!\Gamma(n+k+1)}$

where δ_{mn} is the Delta-Dirac function, β_m and β_n are different roots of J_p. This is also called the Fourier-Bessel series (Smythe (1939)).

The eq.5.27 must then be multiplied by the weighting function $W(r) = r$, and another Bessel function J_0 with a different root β_m, and then integrated over r. Thus,

$$\begin{aligned}
\sum_{n=1}^{\infty} d \int_0^b \frac{r}{b} J_0(\beta_m \frac{r}{b}) J_0(\beta_n \frac{r}{b}) dr &= \int_0^b \frac{r}{b} T_0 J_0(\beta_m \frac{r}{b}) dr \,, \\
\sum_{n=1}^{\infty} d \frac{1}{b} \frac{b^2}{2} J_1(\beta_n)^2 &= \frac{T_0}{b} \int_0^b r J_0(\beta_m \frac{r}{b}) dr \,, \\
\sum_{n=1}^{\infty} d \frac{1}{b} \frac{b^2}{2} J_1(\beta_n)^2 &= \frac{T_0}{b} \frac{b^2 J_1(\beta_m)}{\beta_m} \,, \\
\implies d_n &= \frac{2T_0}{\beta_n J_1(\beta_n)} \,. \qquad (5.28)
\end{aligned}$$

The constants from the expression for temperature in eq.5.25, C and d, are now found.

From the thermal diffusion equation in eq.5.19, we have now obtained an expression for the temperature in a 2D-cylindrical case, with a uniform initial temperature distribution T_0 inside, and the outside temperature equal to zero, and an other radius b,

$$T(r,t) = T_0 \sum_{n=1}^{\infty} \frac{2}{\beta_n J_1(\beta_n)} J_0\Big(\beta_n \frac{r}{b}\Big) e^{-\kappa \frac{\beta_n^2}{b^2} t} \,. \qquad (5.29)$$

For a case with an outside temperature $T_1 \neq 0$, the equation above must be modified with setting $(T_0 - T_1)$ instead of T_0.

5.1.3 Thermal stress in a cylinder

The expressions for the stresses found in eq.5.14, 5.15 and 5.16, needs the integral over $T(r,t)r$, and from eq.5.29 we see that the parts in $T(r,t)$ depending on r gives,

$$\begin{aligned}
\int_0^b J_0(\beta_n \frac{r}{b}) r dr &= \frac{b^2}{\beta_n} J_1(\beta_n) \,, \quad \text{and} \\
\int_0^r J_0(\beta_n \frac{r}{b}) r dr &= \frac{br}{\beta_n} J_1(\beta_n \frac{r}{b}) \,.
\end{aligned}$$

Inserting the temperature from eq.5.29 in the radial stress gives,

$$\begin{aligned}
\sigma_r &= \frac{\alpha E}{1-\nu} \left(\frac{1}{b^2} \int_0^b T r dr - \frac{1}{r^2} \int_0^r T r dr \right) \,, \\
&= \frac{\alpha E}{1-\nu} \left[\frac{1}{b^2} T_0 \sum_{n=1}^{\infty} \frac{2}{\beta_n J_1(\beta_n)} e^{-\kappa \frac{\beta_n^2}{b^2} t} \frac{b^2}{\beta_n} J_1(\beta_n) - \frac{1}{r^2} T_0 \sum_{n=1}^{\infty} \frac{2}{\beta_n J_1(\beta_n)} e^{-\kappa \frac{\beta_n^2}{b^2} t} \frac{br}{\beta_n} J_1(\beta_n \frac{r}{b}) \right] \\
&= \frac{2\alpha E T_0}{1-\nu} \sum_{n=1}^{\infty} \frac{1}{\beta_n^2} e^{-\kappa \frac{\beta_n^2}{b^2} t} \left(1 - \frac{b}{r} \frac{J_1(\beta_n \frac{r}{b})}{J_1(\beta_n)} \right) \,. \qquad (5.30)
\end{aligned}$$

For σ_θ we get,

$$\begin{aligned}\sigma_\theta &= \frac{\alpha E}{1-\nu}\left(\frac{1}{b^2}\int_0^b Trdr - \frac{1}{r^2}\int_0^r Trdr - T\right), \\ &= \frac{2\alpha E T_0}{1-\nu}\sum_{n=1}^{\infty} e^{-\kappa\frac{\beta_n^2}{b^2}t}\left(\frac{1}{\beta_n^2} + \frac{1}{\beta_n^2}\frac{b}{r}\frac{J_1(\beta_n\frac{r}{b})}{J_1(\beta_n)} - \frac{1}{\beta_n}\frac{J_0(\beta_n\frac{r}{b})}{J_1(\beta_n)}\right). \end{aligned} \tag{5.31}$$

The axial stress gives,

$$\begin{aligned}\sigma_z &= \frac{\alpha E}{1-\nu}\left(\frac{2\nu}{b^2}\int_0^b Trdr - T\right), \\ &= \frac{2\alpha E T_0}{1-\nu}\sum_{n=1}^{\infty} e^{-\kappa\frac{\beta_n^2}{b^2}t}\left(\frac{2\nu}{\beta_n^2} - \frac{1}{\beta_n}\frac{J_0(\beta_n\frac{r}{b})}{J_1(\beta_n)}\right). \end{aligned} \tag{5.32}$$

These expressions are valid for a plain strain assumption.

We have now analytical expressions for thermally induced stress in a cylindrical domain, and it is now possible to validate the numerical models.

5.2 Benchmarking of the numerical models

The two-dimensional finite element model and the one-dimensional finite difference model in polar coordinates can now be tested against the analytical solution derived in the previous section.

Instead of solving the diffusion-reaction equations described in Chapter 2, and discretized in Chapter 4, we have only addressed (thermal) diffusion for this benchmarking. The diffusion equation used is given in Section 5.1.2 in Eq. 5.19, for the two-dimensional model, and in Eq. 5.20, for the cylindrical model.

The equations to be solved for the mechanical model are given in Section 4.2 and 4.3.2, for the two-dimensional and cylindrical model, respectively. The only difference is that the eigenstrain ϵ^* is now the thermal strain $\epsilon^T = \alpha\Delta T$.

The analytical solution derived in the previous sections, addressed the cooling of a cylinder, and how thermal stresses build up while cooling. The parameters are non-dimensionalized. The initial conditions were $T = 1$ inside the domain, and $T = 0$ at the boundary. The material was assumed to be homogenous, with no variations in vertical direction, thus the result can only depend on the radial coordinate r. In the mechanical model a plain strain condition was assumed, the displacement in the center was set to zero, and the radial stress at the surface also set to zero.

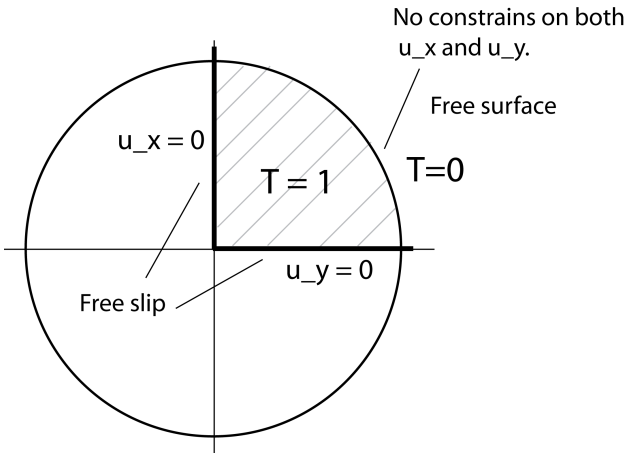

Figure 5.2: The computational domain for the FEM-comparison of the analytical solution.

For the two-dimensional finite element model the setup is shown in Figure 5.2.

In Figure 5.3 an example of the temperature and stress distribution, obtained using the cylindrical FD-model, is shown. Results obtained by the 2D FEM-model are plotted in Figure 5.4. Since three figures are needed to plot the different stress components we choose here to plot for the pressure $p = (\sigma_{xx} + \sigma_{yy} + \sigma_{zz})/3$.

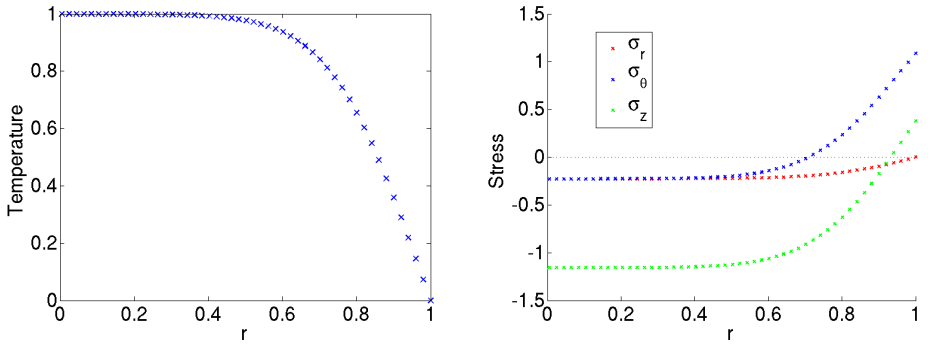

(a) Temperature **(b)** Stress components

Figure 5.3: Examples of profiles in the cylindrical FD model.

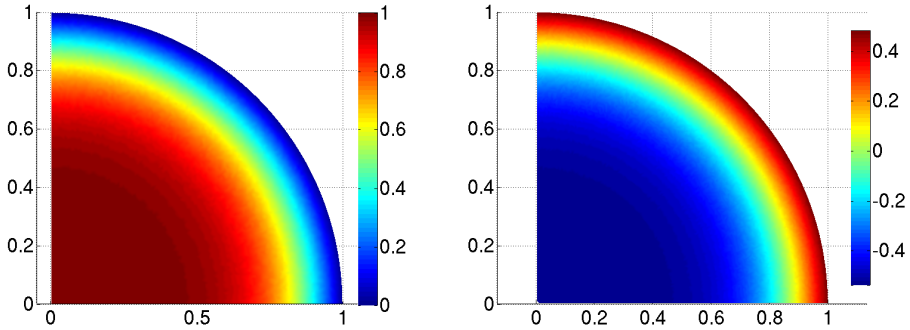

(a) Temperature **(b)** Pressure

Figure 5.4: Examples of profiles in the 2D-FEM model.

Table 5.1: Parameters chosen for the benchmarking.

Youngs modulus E	1	T_0	1
Poissons ratio ν	0.35	T_1	0
Thermal stress coefficient α	1	r_b	1
Thermal diffusivity κ	1		
Time step Δt	0.002	Number of time steps	10
Values for the analytical solution			
Number of Bessel zeros	50	Points for plotting	200
Values for the 2D-FEM model			
Type of elements	Triangles	Shape functions	Linear
Number of elements	∼20000		
Values for the FD-model			
Number of grid points	500		

When comparing the results obtained by the numerical models with the analytical result, the parameters and numerical resolution chosen are given in Table 5.1.

In Figure 5.5 the analytical solution is plotted together with the numerical solutions for the cylindrical finite difference model and the two-dimensional finite element model. One can observe that the curves coincide, and that the models are able to reproduceing the analytical solution. To study the error distribution, we define the difference error for the temperature $\Delta T = T_{\text{Numerical}} - T_{\text{Analytical}}$, and similarly for the three stress components. The error is shown in Figure 5.6.

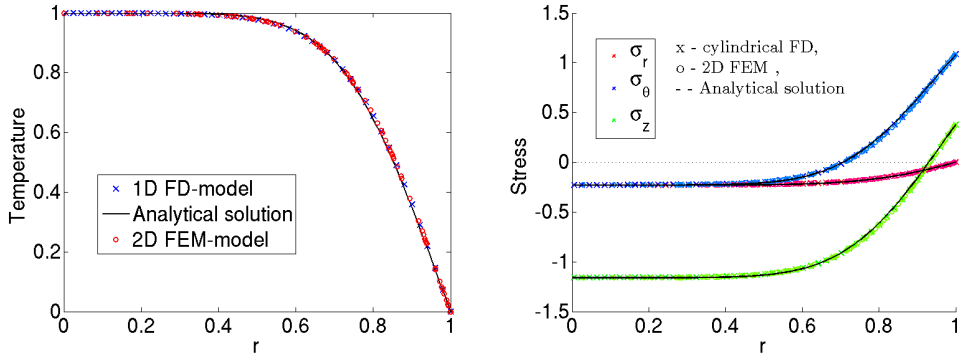

(a) Temperature **(b)** Stresses

Figure 5.5: Plot of the temperature and stress-profiles for both numerically and analytically obtained solutions.

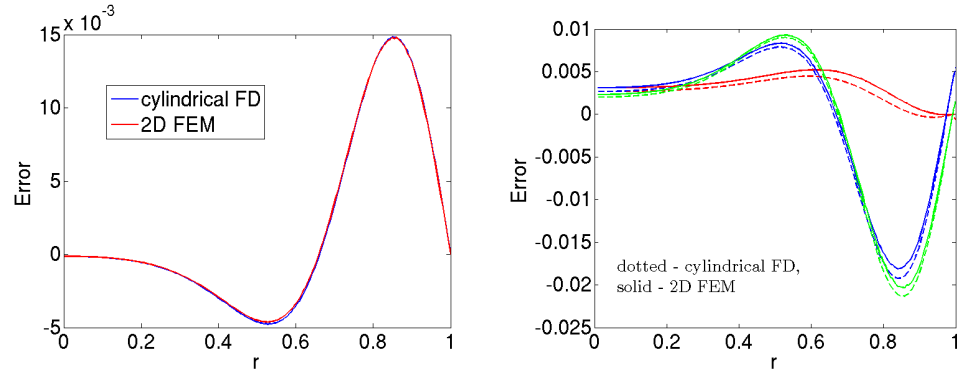

(a) Temperature **(b)** Stresses

Figure 5.6: The error of the numerical models with respect to the analytical solution.

We observe that the two numerical models give almost the exact same error for the temperature, but that there are larger differences between the models in the errors in the stress.

From the maximum error of the temperature it is possible to find the corresponding relative error, $\Delta T/T_{\text{analytical}}$. For both the FD- and the FEM-model this is found to be approximately maximum 2.9%. The maximum percentage error for the stress profiles is found for the σ_θ-profiles, and are for the FD-model approximately 0.51%, and for the FEM-model approximately 0.45%.

The errors occur because the domain is discretized both in time and space, and we have prescribed a Δr and Δt, between which the function values are approximated or interpolated. It is possible to do a convergence test for the numerical models by increasing the resolution, but this was not done in this project. It is also interesting that the error is lower for the stress-profiles than for the temperature profiles, since the temperature is used as input to the mechanical model as the eigenstrain ϵ^T. Nevertheless we will not look more into these problems, since the error is so low.

Chapter 6

Results and Discussion

The model of deformation of peridotite during carbonation can now be studied using the benchmarked numerical models.

To give a quick recapitulation, the model of fluid-rock interaction is approximated by diffusion-reaction, and there is a volumetric effect related to the reaction which induces stress. Three models have been developed for different geometries,

- a one-dimensional model, studying the half-space. One steady state model for the moving reference frame of the reaction front, and one time dependent model where fractures are initiated
- a one-dimensional model of a cylinder, where plain strain and axis-symmetry is assumed,
- a two-dimensional model with rectangular domain, assuming plain strain. Also a geometry from real data is approached

In the one-dimensional, time dependent model, the fracture criterion of Rudge et al. (2010) is used, and a comparisson of the result of Rudge et al. (2010) is done.

The cylindrical model is developed to study how the stresses behave on a cylindrical domain. The Coulomb fracture criterion is used to predict when the material will fail.

For the two-dimensional model, it is interesting to study the stress field, as the reaction proceed inwards in a material with a different geometry than a cylinder. Geometries from real-data is also studied.

6.1 Reproducing Rudge

In the model of Rudge et al. (2010), the main objective was to determine the front velocity and the typical fracture length as a function of given parameters. A detailed dimensional analysis was performed for the steady state problem (Eq.2.6-2.11), together with the fracture criterion (Eq.2.18), and they found two governing non-dimensional parameters Λ and Θ, defined by,

$$\Lambda = \frac{\kappa}{D}\Big(\frac{K_c}{\beta E}\Big)^4 , \quad \Theta = \frac{w_0}{rb_0} .$$

The symbols are defined in Chapter 2. The non-dimensional front velocity and crack length were then found as functions of these two parameters. The non-dimensional front velocity was defined by,

$$\eta(\Lambda, \Theta) = \frac{v}{D}\Big(\frac{K_c}{\beta E}\Big)^2 ,$$

where v is the front velocity. The non-dimensional crack length was defined by,

$$\xi(\Lambda, \Theta) = L\Big(\frac{\beta E}{K_c}\Big)^2 ,$$

where L is the crack length.

In Chapter 4, Section 4.1 the discretization of the steady state problem in one-dimension is done. The boundary values from the Equations (2.6-2.11) are used, and the problem is solved on a large domain, thus the steady state distribution will not be affected by boundary effects.

To find the steady state distribution of the concentration, the relaxation iterative method was used. The algorithm is described in Section 4.1. The number of iterations was set to $n_r = 1000$, for an $\alpha = 0.05$. This was a sufficiently low α to aviod numerical instabilities, and a high enough n_r to reach a steady state.

The problem were solved for different parameters to achieve a range of the non-dimensional numbers Λ and Θ between 0 and 3. However there is a non-uniform scaling between the dimensional and non-dimensional parameters, and it is difficult to obtain a uniform distribution of in the space of Λ and Θ. The non-dimensonal front velocity η and crack length ξ were calculated for the values of Λ and Θ obtained, and then interpolated to achieve the range between 0 and 3 which were used by Rudge et al. (2010).

The result obtained for $\eta(\Lambda, \Theta)$ is shown in Figure 6.1(a), and in the (b)-part the result obtained in the article of Rudge et al. (2010) is shown. One can observe that the two results are similar.

The result for the non-dimensional crack length $\xi(\Lambda, \Theta)$ is given in Figure 6.2 together with the plot from Rudge et al. (2010). For the crack length one can observe that the result is reproduced to the extent it is possible to compare these two figures.

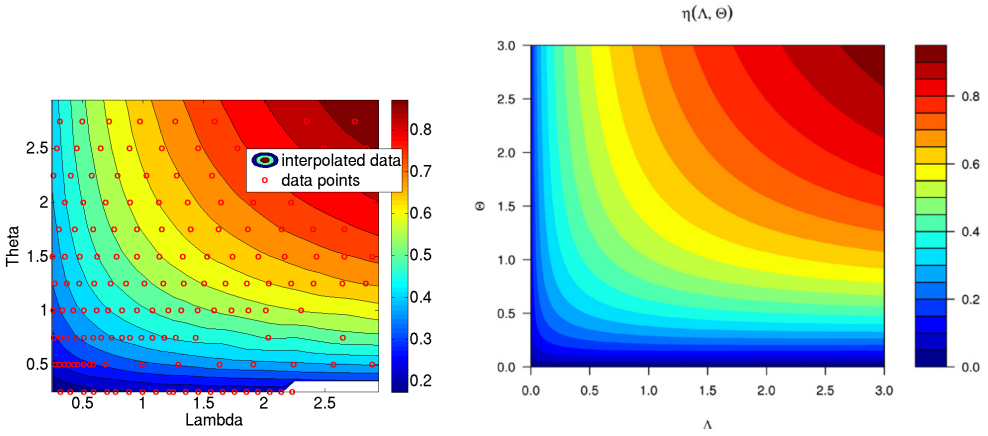

(a) $\eta(\Lambda, \Theta)$, obtained from the steady state model

(b) $\eta(\Lambda, \Theta)$, from Rudge et al. (2010) (Fig.2)

Figure 6.1: Plot of the non-dimensional front velocity $\eta(\Lambda, \Theta)$.

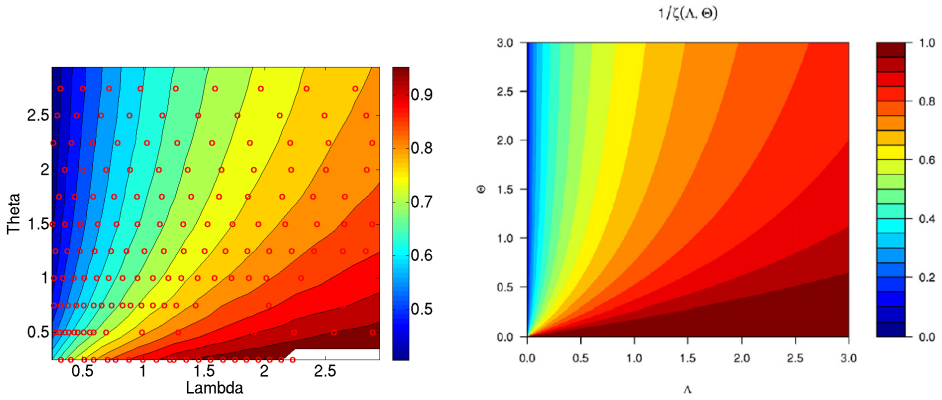

(a) $1/\xi(\Lambda, \Theta)$, obtained from the steady state model

(b) $1/\xi(\Lambda, \Theta)$, from Rudge et al. (2010) (Fig.3)

Figure 6.2: Plot of the inverse non-dimensional crack length $1/\xi(\Lambda, \Theta)$.

6.1.1 Comparing the transient solution with the steady state solution

The steady state model used in the previous section is derived from the time dependent diffusion-reaction model in Eq. (2.2-2.4), with the assumption that front is moving with a constant velocity, and solves the diffusion-reaction problem in the moving reference frame of the front.

If the transient problem is modeled instead, it is possible to find the non-dimensional front velocity and crack length, and compare with the results obtained by the steady state model. The transient problem is investigated because there will not exist a propagating front, in steady state, when other geometries,

such as a cylinder or a rectangular, are studied. The differences between the steady state and the time dependent model are interesting to study, before making use of the time dependent model on other geometries.

A brief recapitulation of the problem is presented to describe how the front velocity can be calculated in the transient model. The Equations in (2.2-2.4) govern the evolution of the concentrations to the different solid phases, A and B as the mobile phase W diffuses inwards and is reacting with A. The production of B produces stresses, and as discussed in Section 2.6, a fracture will occur if the stress intensity factor K exceeds the critical stress intensity factor K_C of the material. The concentration of B, given by b, produces the stress,

$$\sigma(x) = \beta E b(x)/b_0$$

and the stress intensity factor is defined by,

$$K = \sigma(0)L^{1/2} ,$$

where L is the crack length, defined by the length of the e-fold decrement of σ from the front, or from the last opened fracture. A fracture is postulated to open if $K >= K_C$. When the transient problem is solved, the crack length L must be calculated, and the fracture criterion must be tested for each timestep.

In Figure 6.3(a) the concentration of the diffusive water w and the concentration of the produced solid phase b are plotted for a given time. The green circle indicates the e-fold decrement of b, hence the position of the e-fold decrement of the stress σ, and the distance from the front to the green circle is the crack length L. When the fracture criterion is fulfilled, the material is 'opened' over the distance L, and the mobile phase is moved instantaneously over the fracture. The concentration of W in the new position of the front is then $w = w_0$ directly after a fracture has occured.

In Figure 6.3(b) the concentrations are shown for a later time, and four fractures have opened. With time the front will proceed in the same manner with a constant velocity. The time for the first fracture to occur is different than between the rest of the fractures, because the concentration b is initially zero. This time period is also called the 'transient', and is the time before a steady state is reached. Hence the front velocity is calculated as the time it takes for the second fracture to occur, with respect to when the first fracture occured. The crack length is then the distance between the first and the second fracture. With respect to the front velocity, it is not necessary to do calculation in the already fractured rock, hence the calculations are stopped in the area behind the front.

The non-dimensional front velocity is calculated for the range of the non-dimensional parameters Λ and Θ between 0 and 3, and the result is shown in Figure 6.4(a). Compared to the profiles found by Rudge et al. (2010) in Figure 6.1(b), the shape is the same, but the values are somewhat different. One could imagine that a simple scaling between the two profiles would exist. However in Figure 6.4(b) the ratio $\eta_{\text{transient}}/\eta_{\text{steady state}}$ is shown. Where $\eta_{\text{transient}}$ is the non-dimensional front velocity obtained from the time dependent model, and $\eta_{\text{steady state}}$ is the one obtained from the steady-state model. One can observe that there exist a non-trivial scaling, with values from approximately 1.5 to 2.

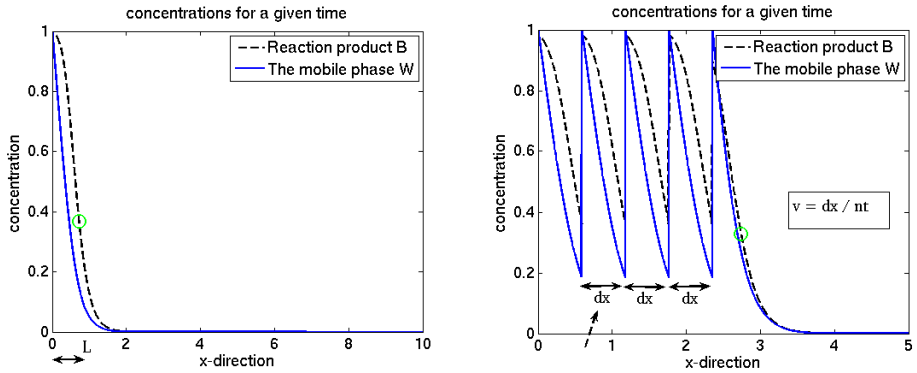

(a) Defining the crack length

(b) Defining the front velocity

Figure 6.3: How the crack length L (a), and the front velocity (b) is defined for the transient solver.

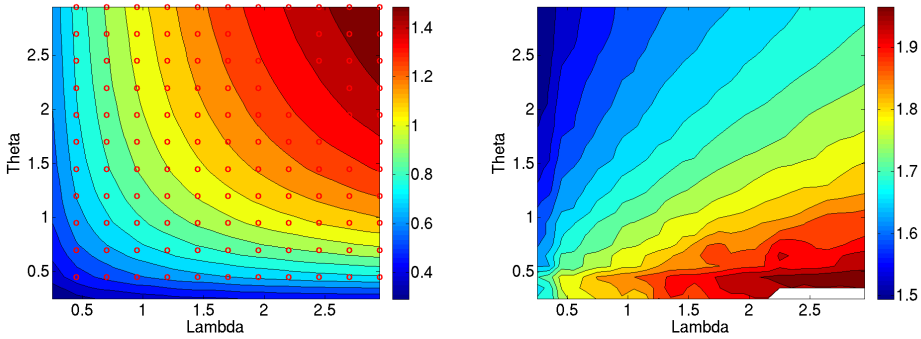

(a) $\eta(\Lambda, \Theta)$, obtained from the transient model

(b) The ratio $\eta_{\text{transient}}/\eta_{\text{steady state}}$

Figure 6.4: Plot of the non-dimensional front velocity $\eta(\Lambda, \Theta)$. (a) shows the results obtained from the time dependent model, and (b) shows the ratio of the results from the transient-, over steady state model.

In Figure 6.5(a) the non-dimensional crack length calculated in the time dependent model is plotted for the non-dimensional parameters Λ and Θ. Compared to the crack length found by Rudge et al. (2010), given in the Figure 6.2(b), the profiles are similar. The ratio between them is plotted in Figure 6.5(b), and the ratio is between $\sim 1 - 0.9$ for most of the plot. This indicates that the time dependent model is able to some degree reproduce the non-dimensional crack length from the steady state model.

Compared to the results of Rudge et al. (2010), we get a higher front velocity using the transient model, but we are (almost) able to get the same result of the crack length. This could be due to the fact that we are actually moving the front the full crack length L whenever a fracture occur, but in the steady state model

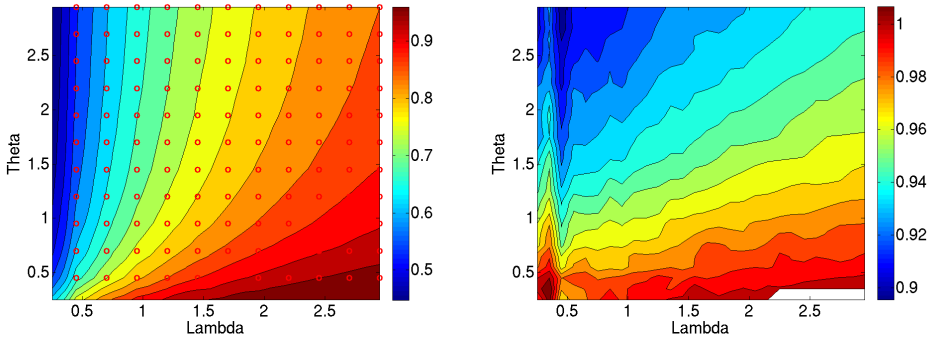

(a) $\xi(\Lambda, \Theta)$ obtained from the transient model

(b) The ratio $\xi_{\text{transient}}/\xi_{\text{steady state}}$

Figure 6.5: Plot of the non-dimensional crack length $\xi(\Lambda, \Theta)$. (a) shows the results obtained from the time dependent model, and (b) shows the ratio of the results from the transient-, over steady state model.

the front is moved continuously. The variations between the result obtained from the transient and the steady state model for the front velocity, in Figure 6.4(b), can indicate that η is somewhat dependent on the crack length shown in Figure 6.5(a). To achieve a better result on the non-dimensional front velocity one could try to not move the front the whole crack length L, whenever a fracture occur. Since the fracture criterion used in this one-dimensional model not will be used in the following models for other geometries, we will not consern ourself with this problem further.

In the next sections the models of the cylindrical and the two-dimensional domain will be studied, with use of the transient solver without the fracture criterion used above.

6.2 Stresses in a cylinder

The discretization of the one-dimensional model in polar coordinates is given in Section 4.3. Here the diffusion-reaction equations are the same as for transient one-dimensional model used in the previous section. The eigenstrain produced from the volume change from A to B is also here given as $\epsilon^* = \beta b(r)/b0$, but we will solve for all the stress components, $\sigma_r,\ \sigma_\theta,\ \sigma_z$, as described in Section 4.3.2.

The Coulomb failure criterion, discussed in Section 2.6.1, will be used,

$$\sigma_3 = -C_u + \left[(1+\mu_i^2)^{1/2} + \mu_i\right]^2 \sigma_1 \ , \tag{6.1}$$

where σ_1 and σ_3 are the major and minor principal stresses, respectively. The intermediate principal stress σ_2 do not contribute to this criterion. The internal friction coefficient μ_i and the uniaxial compressive strength C_u are material parameters. The Eq. 6.1 describes the failure surface in the principal stress space, and when considering this criterion one must also take into account the uniaxial tensile strength T_u, see Figure 2.6. The rule-of-thumb for the ratio between the uniaxial compressive- and tensile strength is that $C_u \approx 8T_u$, although this can vary within a factor or two for laboratory measured rock samples (Pollard and Fletcher (2005)). If the compressive strength is prescribed, failure will occur if the tensile stress exceeds $C_u/8$. Thus the criterion in Eq. 6.1, together with the tensile stress check is needed for a full failure criterion.

6.2.1 Dimensional analysis

The diffusion-reaction model in polar coordinates is given,

$$\begin{aligned}
\frac{\partial w}{\partial t} &= D\frac{1}{r}\frac{\partial}{\partial r}\Big(r\frac{\partial w}{r}\Big) - \rho k w a \\
\frac{\partial a}{\partial t} &= -s k w a \\
\frac{\partial b}{\partial t} &= k w a \ ,
\end{aligned}$$

together with the boundary and initial conditions,

$$\begin{aligned}
w(r_b,t) = w_0 \quad w(r,1) &= 0 \ , \ r \in [0, r_b) \\
a(r,1) &= a_0 \ , \ r \in [0, r_b] \\
b(r,1) &= 0 \ , \ r \in [0, r_b]
\end{aligned}$$

over the spatial domain $r \in [0, r_b]$, and the time domain $t \in [0, t_1]$. The dimensions of the variables are given in Section 2.2. A b_0 is defined as $b_0 = a_0/s$, and is the amount of b if all of a was reacted.

The rescaled concentrations are obtained by $w' = w/w_0$, $a' = a/a_0$ and $b' = b/b_0$. The spatial coordinate is rescaled by $r' = r/r_b$, and for the time we choose to scale

like $t' = t/(r_b^2/D)$. The new dimensionless-form of the diffusion-reaction model is then,

$$\begin{aligned}
\frac{\partial w'}{\partial t'} &= \frac{1}{r'}\frac{\partial}{\partial r'}\left(r'\frac{\partial w'}{r'}\right) - \Gamma w' a' \\
\frac{\partial a'}{\partial t'} &= -\Gamma\Omega w' a' \\
\frac{\partial b'}{\partial t'} &= \Gamma\Omega w' a' \,,
\end{aligned}$$

where we have defined two non-dimensional parameters governing the system,

$$\Gamma = \frac{r_b^2 a_0 k\rho}{D} \,,$$

and,

$$\Omega = \frac{s w_0}{\rho a_0} \,.$$

The parameter, Γ is a competition between the reaction constant k, the size of the domain r_b and the diffusion constant D. A high Γ means a large domain size and/or reaction constant compared to the diffusion constant, thus a more rapid reaction than diffusion. While a low Γ means a large diffusion constant compared to domain size and/or reaction constant, and hence a more rapid diffusion than reaction.

The non-dimensional parameter Ω involves the ratio over the stoichiometric coefficients, and the ratio of the concentration w (eg. water) at the boundary, over the initial concentration a (eg. peridotite). A high Ω would mean that the rock is porous, and a low Ω a dense rock, with low porousity.

The equations for the mechanical model are discussed in Section 4.3.2, and we solve for the displacement,

$$\frac{\partial^2 u}{\partial r^2} + \frac{1}{r}\frac{\partial u}{\partial r} - \frac{1}{r^2}u = \frac{1+\nu}{1-\nu}\frac{\partial \epsilon^*}{\partial r} \,.$$

To non-dimensionalize on the displacement the r is scaled like before, $r' = r/r_b$. Observe that the eigenstrain $\epsilon^* = \beta b(r)/b_0$, already is on non-dimensionless form when we introduce the scaling for b used above $b' = b/b_0$, thus $\epsilon^*_{\text{nondim}} = \beta b'(r')$. For the displacement u, we scale with $u' = u/r_b$. Introducing these rescaled functions gives,

$$\frac{\partial^2 u'}{\partial (r')^2} + \frac{1}{r'}\frac{\partial u'}{\partial r'} - \frac{1}{(r')^2}u' = \frac{1+\nu}{1-\nu}\frac{\partial}{\partial r'}(\epsilon^*_{\text{nondim}}) \,.$$

The displacement is now used to calculate the stress components. If the same scales are introduced in the equations for the stress, and the stress is scaled with Youngs modulus E, we get,

$$\begin{aligned}
\frac{\sigma_r}{E} &= \frac{1}{(1+\nu)(1-2\nu)}\left[(1-\nu)\frac{\partial u'}{\partial r'} + \nu\frac{u'}{r'} - \epsilon^*_{\text{nondim}}(1+\nu)\right] \,, \\
\frac{\sigma_\theta}{E} &= \frac{1}{(1+\nu)(1-2\nu)}\left[\nu\frac{\partial u'}{\partial r'} + (1-\nu)\frac{u'}{r'} - \epsilon^*_{\text{nondim}}(1+\nu)\right] \,, \\
\frac{\sigma_z}{E} &= \nu(\sigma_r/E + \sigma_\theta/E) - \epsilon^*_{\text{nondim}} \,.
\end{aligned} \tag{6.2}$$

The Coulomb criterion given in Eq. 6.1 is also scaled with Youngs modulus to achieve a non-dimensional form,

$$\frac{\sigma_3}{E} = -\frac{C_u}{E} + \left[(1+\mu_i^2)^{1/2} + \mu_i\right]^2 \frac{\sigma_1}{E}\,, \tag{6.3}$$

If we recognize σ_r as the tensile principal stress σ_1, and σ_z as the minor compressive principal stress σ_3, we can rewrite the Coulomb criterion in Eq. 6.3 with the expression in Eq. 6.2, to find,

$$\frac{1}{(1+\nu)(1-2\nu)}\left[\frac{\partial u'}{\partial r'}\Big(\mu_i^E(1-\nu)-\nu\Big) + \frac{u'}{r'}\nu\Big(\mu_i^E-1\Big)\right] + \epsilon^*_{\text{nondim}}\left[\frac{1-\mu_i^E}{1-2\nu}\right] - \frac{Cu}{E} = 0$$

where $\mu_i^E = \left[(1+\mu_i^2)^{1/2} + \mu_i\right]^2$. If we insert for the $\epsilon^*_{\text{nondim}}$, and divide by β we get,

$$\frac{1}{(1+\nu)(1-2\nu)}\frac{1}{\beta}\left[\frac{\partial u'}{\partial r'}\Big(\mu_i^E(1-\nu)-\nu\Big) + \frac{u'}{r'}\nu\Big(\mu_i^E-1\Big)\right] + b'(r')\left[\frac{1-\mu_i^E}{1-2\nu}\right] - \frac{Cu}{E}\frac{1}{\beta} = 0\,. \tag{6.4}$$

Recall that β relates to the relative volume change obtained from the reaction. We define the last term in the Coulomb criterion in Eq. 6.4 as,

$$Ha = \frac{Cu}{E}\frac{1}{\beta} = \frac{Cu}{E}3(1-\nu)\Big(\frac{dV}{V}\Big)^{-1}\,.$$

The non-dimensional parameter Ha is now a relation between the strength of the material, and the relative volume change it will feel from the chemical reactions. A high value on Ha will mean a strong material compared to the relative volume change, and a low Ha will mean a big volume change and a weaker material. The value of Ha will not be prescribed, but used as an indicator after β and C_u/E have been defined. Since there is a β-term in the first term in Eq. 6.4, the number Ha is not completely independent.

To find the physical range of the non-dimensional numbers, the real values of the originally parameters needs to be discussed. In Rudge et al. (2010) they discussed what others have found from experiments and field investigations. Amoung other things the values were based on studies of grain-sizes and porespace, partial pressure of carbon dioxide, porefluid pressure, temperature, etc. . In the following we will go through the numbers chosen in Rudge et al. (2010).

Recall the reaction rate $\kappa = skw_0$ from Section 2.2, this is found to be approximately $\kappa_{serp.} \sim 5 \times 10^{-11} s^{-1}$ for serpentinization, and $\kappa_{carb.} \sim 2.5 \times 10^{-10} s^{-1}$ for carbonation. The porosity is estimated to be $\phi \sim 3 \times 10^{-4}$, and we use this estimate for the ratio of the concentration of W and A, or how much water the host rock can contain, $w_0/a_0 \sim 3 \times 10^{-4}$. The diffusivity is $D \sim 3 \times 10^{-14} m^2 s^{-1}$. The stoichiometric coefficients s and ρ is simply set to

$s = \rho = 1$. By assuming these parameters the non-dimensional variable Γ becomes,

$$\Gamma \approx \frac{r_b^2\, 10^{-11} 10^4}{10^{-14}} = r_b^2\, 10^7 \,,$$

interesting domain sizes are of orders 1 meter to 1 mm, thus $r_b \sim 10^0 m - 10^{-3} m$, which gives the range of $\Gamma \sim 10^2 - 10^7$. The parameter Ω is given by the concentration ratio and stoichiometric coefficient, and we set $\Omega \approx 10^{-4}$. The relative volume change between the host rock and the reaction product B, is set to be approximately $dV/V \sim 0.1\% - 1.0\%$.

For the mechanical properties of the rock parameters have been found in Pollard and Fletcher (2005). The Poisson's ratio is set to $\nu \approx 0.25$. The internal friction coefficient is chosen to be between $\mu_i \approx 0.5 - 1.4$, from experimental data. The ratio between the uniaxial compressive strength and Youngs modulus is approximately $C_u/E = 1/300$, but varies from $1/200 - 1/1000$ in laboratory experiments. The ratio between the uniaxial compressive strength and the uniaxial tensile strength is, as mentioned previously, $C_u/T_u \approx 8$, and varies by a factor of 2 to 3 in laboratory experiments.

In Table 6.1 the parameters we choose to use are given.

Table 6.1: Parameters for the coupled reaction-diffusion and mechanical model

Compressive-tensile ratio C_u/T_u	8 - 20	Internal friction coef. μ_i	0.5-1.4
Compressive-Youngs ratio C_u/E	1/200 - 1/1000	Poisson's ratio ν	0.25
Relative volume change dV/V	0.1% - 1.0%		
Diffusion constant D	10^{-12} [m^2/s]		
Reaction rate constant κ	10^{-11} [s^{-1}]	Γ	$10^2 - 10^7$
Domain size r_b	10^{-2} - 10^0 [m]		
Concentration ratio w_0/a_0	10^{-4}	Ω	10^{-4}

6.2.2 Results

The non-dimensionalizing of the problem performed above, left us with these equations describing the diffusion-reaction model,

$$\begin{aligned}
\frac{\partial w'}{\partial t'} &= \frac{1}{r'}\frac{\partial}{\partial r'}\left(r'\frac{\partial w'}{r'}\right) - \Gamma w' a' \\
\frac{\partial a'}{\partial t'} &= -\Gamma\Omega w' a' \\
\frac{\partial b'}{\partial t'} &= \Gamma\Omega w' a' \,,
\end{aligned}$$

where $\Gamma = \frac{r_b^2 a_0 k \rho}{D}$, and $\Omega = \frac{s w_0}{\rho a_0}$. From the numbers found in Table 6.1, Ω is prescribed, and the only parameter we can vary is Γ. In Figure 6.6 the concentration profiles w' and b' are plotted for two different values of Γ, and for

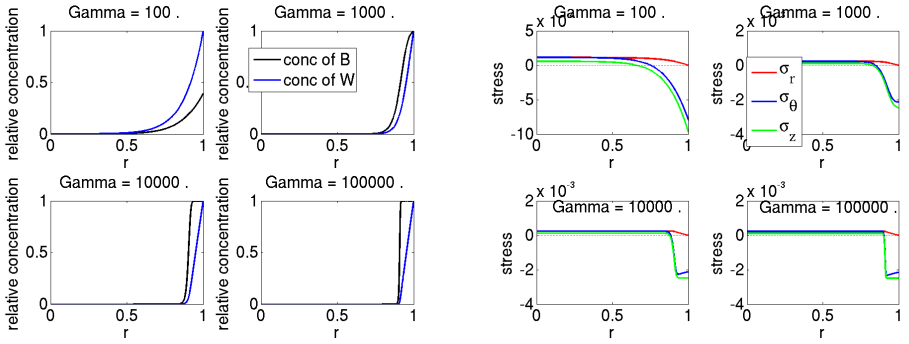

(a) Concentrations profiles

(b) Stress profiles

Figure 6.6: Examples of variations of the non-dimensional parameter Γ.

a non-dimensional time of $t' = 100$. In the same figure the stress components are also plotted. We observe that the a $\Gamma = 10^2$ gives a very diffusive front and that a $\Gamma = 10^5$ gives a very sharp front.

The Coulomb fracture criterion on dimensionless form was found to be,

$$\frac{1}{(1+\nu)(1-2\nu)}\frac{1}{\beta}\left[\frac{\partial u'}{\partial r'}\left(\mu_i^E(1-\nu)-\nu\right)+\frac{u'}{r'}\nu\left(\mu_i^E-1\right)\right]+ b'(r')\left[\frac{1-\mu_i^E}{1-2\nu}\right]-Ha=0\,. \tag{6.5}$$

where the last term were defined as $Ha = \frac{Cu}{E}\frac{1}{\beta}$. Together with the fracture criterion in tensile stress, that is that failure will occur if the tensile stress exceeds $C_u/8$, we can now predict when the material will fail for different sets of parameters.

To visualize how the concentration of the reaction product B, the two failure criterions behave with time, the profiles are plotted with time along the vertical axis, the posistion r along the horizontal axis, and the values as color coded.

In Figure 6.7 profiles are shown for a set of parameters given in the figure caption. In the lower left figure in the subplot, the tensile criterion is fulfilled inside the red line, and the Coulomb criterion is fulfilled within the blue line. We observe that there in this case the Coulomb criterion will first be fulfilled, and that the fracture would initiated approximately 5mm inside the material.

In Figure 6.8 profiles are shown for a higher ratio of C_u/T_u, thus the tensile strength of the material is stronger. Here only the Coulomb criterion is fulfilled. What happens after the first time the fracture criterion is fulfilled is not really interesting, since then possibly a fracture has occured, and the stress state are changed.

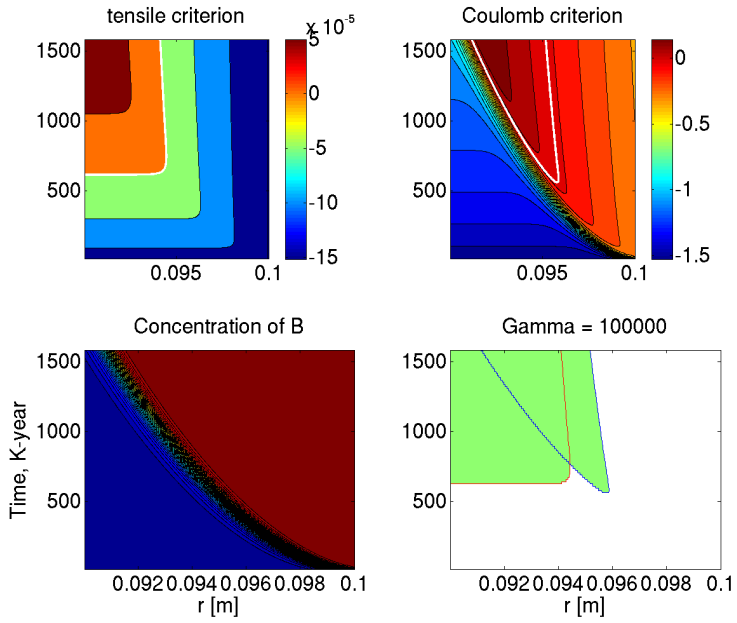

Figure 6.7: Stress criterion for $\Gamma = 100000$, $C_u/T_u = 22$, $C_u/E = 1/300$, $Ha = 1.5625$.

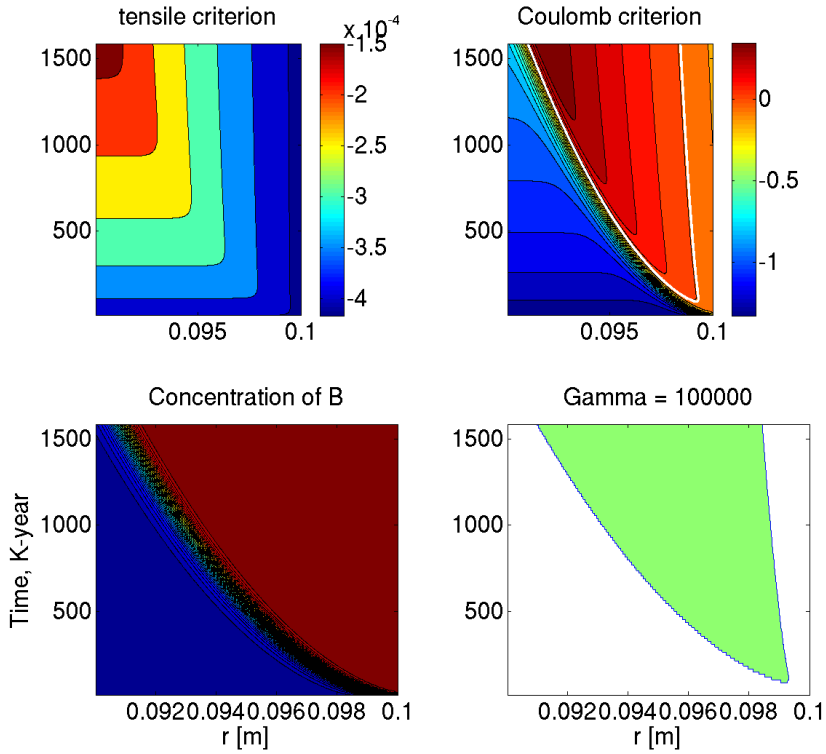

Figure 6.8: Stress criterion for $\Gamma = 100000$, $C_u/T_u = 8$, $C_u/E = 1/300$, $Ha = 1.3636$.

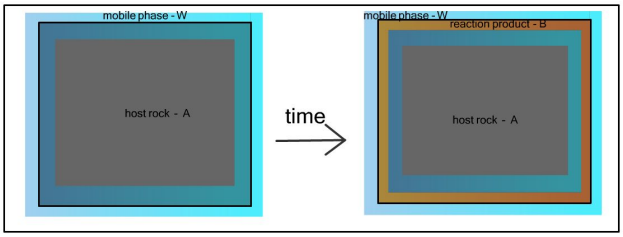

Figure 6.9: Simple model setup of the reaction-diffusion model.

6.3 Stress on a two-dimensional domain

In Chapter 2 the physical problem of chemical weathering processes coupled with deformation, was motivated and discussed. The Figure 2.3 is reprinted in Figure 6.9, and was the illustration of how the numerical model would look like. The two-dimensional diffusion-reaction model coupled with deformation, which was discretized in Section 4.2, can be used to study the problem on a similar domain as shown in the illustration.

When presenting concentration profiles and stress fields in a two-dimensional domain there is need for one figure for each component. Hence we choose to only present the concentration profile of the reaction product B, which produces the eigenstrain ϵ^*. For the stress fields the octhahedral shear stress is chosen to be presented. Recall the expression derived in Section 2.5,

$$\tau_{oct}^2 = \frac{2}{3}J_2 = \frac{2}{3}\frac{1}{6}\Big((\sigma_1-\sigma_2)^2+(\sigma_2-\sigma_3)^2+(\sigma_3-\sigma_1)^2\Big)\,.$$

given in terms of the principal stresses.

It is interesting to observe how the stress field changes with the aspect ratio of the rectangular, and in Figures 6.10-6.12 the concentration profiles of b and the octahedral shear stress is plotted for three different aspect ratios.

We observe that for all the models a high stress concentration is found in the corners, and this can be compared with the results found by Røyne et al. (2008), where they in their model showed that the corners were one of the first part to break off from the full domain. One can also observe that there are patterens in the stress field arising with a higher aspect ratio.

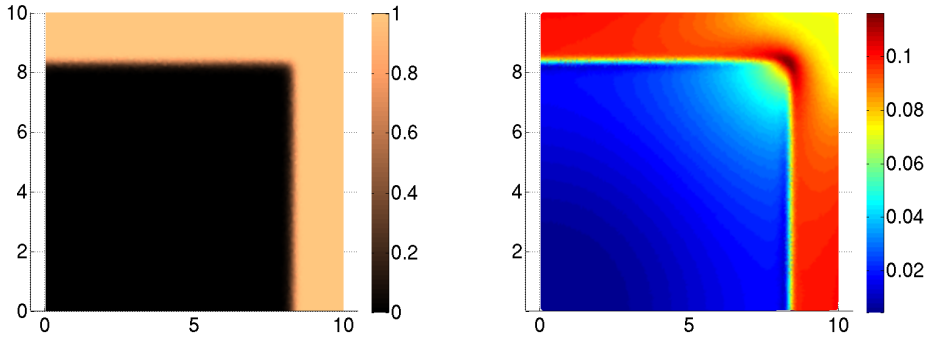

(a) Concentration of B **(b)** τ_{oct}

Figure 6.10: The 2D-numerical model aspect ratio 1.

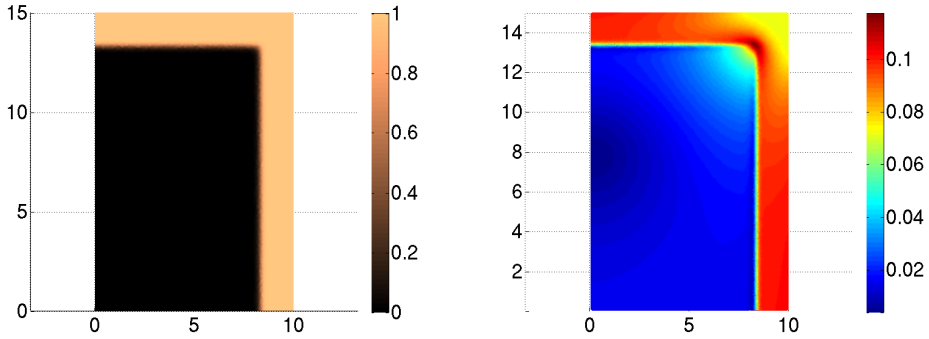

(a) Concentration of B **(b)** τ_{oct}

Figure 6.11: The 2D-numerical model aspect ratio 1.5

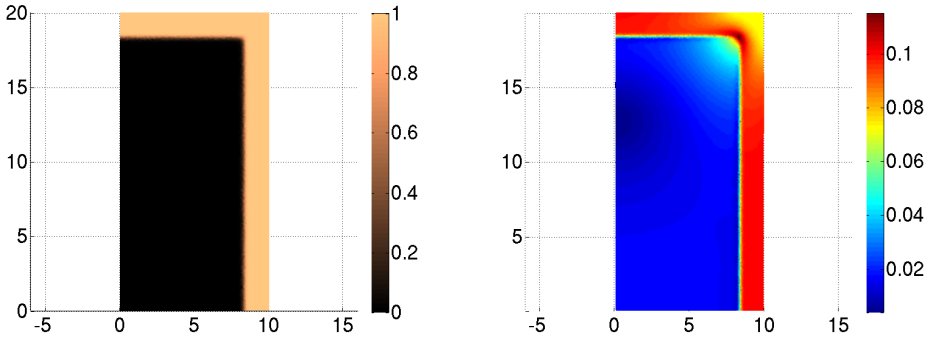

(a) Concentration of B **(b)** τ_{oct}

Figure 6.12: The 2D-numerical model aspect ratio 2.

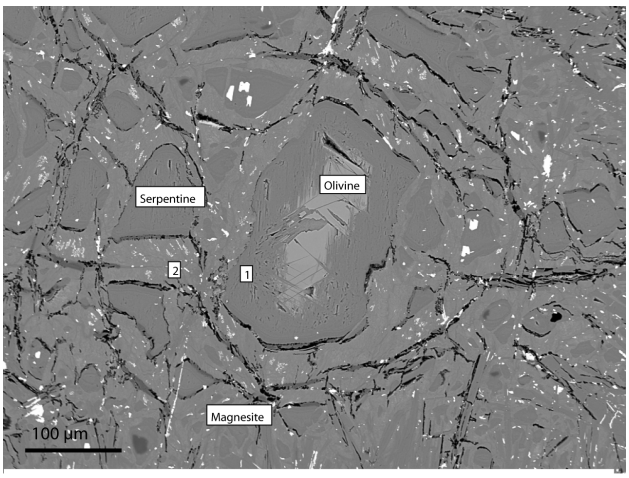

Figure 6.13: SEM from a thin section from the Feragen field complex in Norway. The number 1 and 2, are to mark that there are two different serpentine compositions in the matrix. The magnesite are found in the fractures, and appere as a dark-gray material. Total black means an opened fracture.

6.3.1 Geometries from real data

The backscatter electron image shown in Chapter 1, and reprinted in Figure 6.13, gives an impression of how the microstructur can look like in a peridotite which has been reacting with a fluid. In the olivine grain in the center the reaction has stopped before replacing all of the olivine, and around the grain a lot of radial fractures can be observed. The matrix around are filled with serpentine of different composition and the clasts are of the serpentine 1 (the darker one). Magnesite has mostly been precipitated in the fractures. One can imagine that the fluid has come from all sides in this particular spot, and due to volume changes the material has fractured while the reaction has proceeded.

The scattered mesh around the olivine grain in the middle is not easy to model, but the olivine grain itself is possible. If the serpentine is considered as the reaction product, or the solid phase B, and the olivine is considered as the host rock, solid phase A, we can use the diffusion-reaction model coupled with the mechanical model to study the stresses built up in the grain.

On the small scale of a single grain, we can observe that no intermediate state exists between the olivine and the serpentine, it is either olivine or serpentine. Geo-chemisists explains the process of this small scale to be a dissolution-precipitation process. When the fluid interacts with the rock, it dissolves the primary minerals and the chemical composition of the fluid changes. Then to a point the solution gets supersaturated with respect to a secondary face, and precipitation starts. In the diffusion-reaction model there is no sharp discontinuity between phase A and phase B, it is a continues transition. This could be a conceptual problem with the model on a very small scale. In the model the domain is divided into discrete points or elements, and the continues transition between the two phases can be seen as an averaging over the elements,

or between the discrete points. On large scale it is thus no conceptual problem, because the elements are larger than the smallest grains. The way to get around this problem, and model on the small scale, is to make the transistion between the two phases very sharp. In that way the intermediate stage is only felt by a few elements, and it is possible to say that it is an average in these elements.

Therefore the parameters of the diffusion-reaction solver have been tuned so that the reaction front, or the production of B, is very sharp, and that it can mimic the fully sharp front it should be in nature, while talking about these scales. If one should model the full chemical solution in detail, this would be a whole project in it self. With the coupled reaction and mechanical model the stress-field is calculated.

The input to the two-dimensional finite element model is thus the boundary of the grain with the olivine from the BSE image in Figure 6.13. As an initial value, the fluid concentration w is set to 1 at the boundary, $w_{\delta\Omega} = 1$. For the solid phases there is no concentration of B initially, and the concentration of A is set to 1 in the whole domain, $a_{\Omega} = 1$. The simulation is then run to a time when the concentration of B approximately fit the BSE image's concentration of serpentine. For visualization the second invariant of the deviatoric stress is shown, as discussed in Section 2.5.

In Figure 6.14(a) the BSE image of the olivine grain with the boundary of the grain is shown. The concentration of B is shown in Figure 6.14(b), and this is approximately similar to the serpentine concentration in the BSE image. Although in the BSE image there are many inhomogenities in the serpentine concentration due to small defects in the lattice, and also due to the crystal orientation of the olivine grain. In Figure 6.14(c) the stress field is plotted for the same time.

This is just a 2D-slice in a 3D-rock, but the simulation shows that a two-dimensional model can capture some features for the three-dimensional reality.

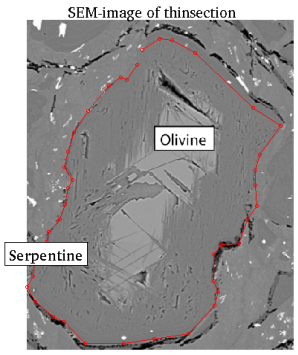

(a) The BSE of the olivine grain.

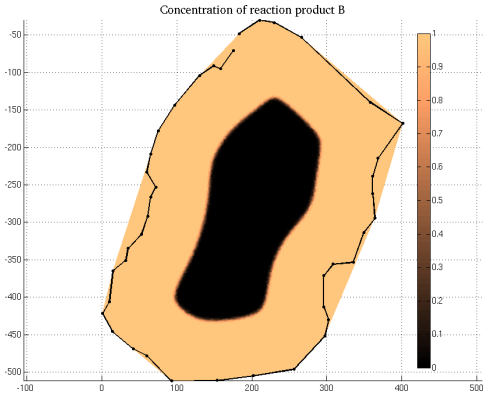

(b) Concentration of B

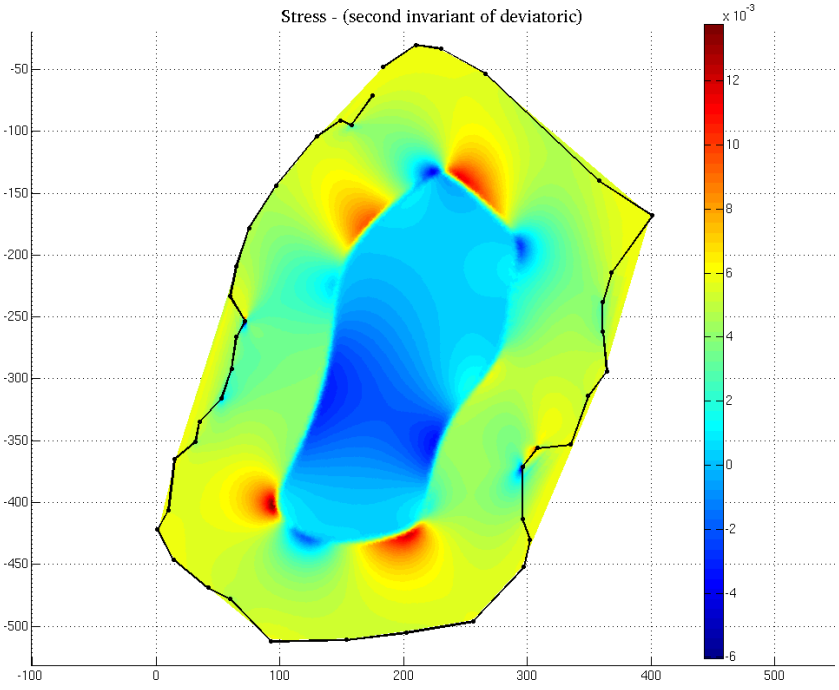

(c) Stresses (second invariant of deviatoric)

Figure 6.14: The 2D-numerical model tested on geometry of a real SEM.

Chapter 7

Concluding remarks

In this Master thesis the problem of chemical weathering are addressed. The study is motivated by the possibilities to store carbon dioxide through mineral carbonation of peridotite. In this respect the thesis is addressing how stresses build up in a material when a volume changing chemical reaction proceeds inwards. Three geometries are studied with numerical models: the half-space domain, a cylindrical domain, and a 2D-rectangulare domain.

The half-space model of Rudge et al. (2010) is reproduced, and compared with a modified version of the problem, to study time-dependency as well. With respect to CO_2-sequestration by mineral carbonation of ultramafic rocks, we can from the steady-state one-dimensional model of Rudge et al. (2010), together with the modified time-dependent model, calculate the front velocity and the rate of carbonation, and the effect of enhancing parameters related to the process.

From the cylindrical model in polar coordinates we have found that a few non-dimensional parameters governs when and how the material will fail, when the Coulomb failure surface was used as a failure criterion. More analysis are needed to possibly find scaling laws for the problem. The field study of spheroidal weathering performed by Røyne et al. (2008), would be one direct application to test the model in polar coordinates with.

This analyses should be extended to the two-dimensional model, to find out more about the effect of the geometry of the material. To a first stage one could study how ellipses with different aspect ratios behaved. It would also be interesting to investigate more geometries from BSE images, to see if the model can reproduce examples from nature.

This Master thesis had a particular focus on geological aspects when it comes to fluid-rock interactions at the Earth's surface. Weathering is also an important problem to understand with respect to culture inheritage of ancient buildings, and building materials in general.

Bibliography

Andreani, M.; Luquot, L.; Gouze, P.; Godard, M.; Hoise, E. and Gibert, B. (2009) *E*xperimental Study of Carbon Sequestration Reactions Controlled by the Percolation of CO2-Rich Brine through Peridotites. Environmental Science and Technology, Vol. 43(4): p. 1226–1231.

Bucher, K. and Frey, M. (2002) *P*etrogenesis of metamorphic rocks (7^{th} edition) (Springer Verlag). Pp. 341.

Coleman, Robert Griffin (1977) *O*phiolites : ancient oceanic lithosphere? / Robert G. Coleman (Springer-Verlag, Berlin ; New York :). ISBN 038708276 354008276 038708276.

Fletcher, C. A. J. (1984) *C*omputational Galerkin Methods (Springer-Verlag).

Fletcher, RC; Buss, HL and Brantley, SL (2006) *A spheroidal weathering model coupling porewater chemistry to soil thicknesses during steady-state denudation*. Earth and Planetary Science Letters, Vol. 244(1-2): p. 444–457.

Fruh-green, GL.; Weissert, H. and Bernoulli, D. (1990) *A multiple fluid history recorded in Alpine ophiolites*. Journal of the Geological Society, Vol. 147(Part 6): p. 959–970.

Fung, Y. C. (1965) *F*oundations of Solid Mechanics (Prentice-Hall, INC.).

Gerdemann, Stephen J.; O'Connor, William K.; Dahlin, David C.; Penner, Larry R. and Rush, Hank (2007) *E*x Situ Aqueous Mineral Carbonation. Environmental Science and Technology, Vol. 41(7): p. 2587–2593.

Giammar, Daniel E.; Jr., Robert G. Bruant and Peters, Catherine A. (2005) *F*orsterite dissolution and magnesite precipitation at conditions relevant for deep saline aquifer storage and sequestration of carbon dioxide. Chemical Geology, Vol. 217(3-4): p. 257 – 276. ISSN 0009-2541. Geochemical Aspects of CO2 sequestering - Geochemical Aspects of CO2 sequestering.

Gislason, Sigurdur Reynir; Wolff-Boenisch, Domenik; Stefansson, Andri; Oelkers, Eric H.; Gunnlaugsson, Einar; Sigurdardottir, Holmfridur; Sigfusson, Bergur; Broecker, Wallace S.; Matter, Juerg M.; Stute, Martin; Axelsson, Gudni and Fridriksson, Thrainn (2010) *M*ineral sequestration of carbon dioxide in basalt: A pre-injection overview of the CarbFix project. International Journal of Greenhouse Gas Control, Vol. 4(3): p. 537 – 545. ISSN 1750-5836.

Griffith, A. A. (1920) *T*he Phenomena of Rupture and Flow in Solids. Philosophical Transaction of the Royal Society of London, Vol. 221: p. 163–198.

Hellan, Kåre (1984) *I*ntroduction to Fracture Mechanics (McGraw-Hill Book Company).

Huijgen, Wouter J.J.; Witkamp, Geert-Jan and Comans, Rob N.J. (2006) *M*echanisms of aqueous wollastonite carbonation as a possible CO2 sequestration process. Chemical Engineering Science, Vol. 61(13): p. 4242 – 4251. ISSN 0009-2509. The John Bridgwater Symposium: 'Shaping the Future of Chemical Engineering'.

IPCC (2005) *S*ummary for Policymakers. In *I*PPC Special report on Carbon Dioxide Capture and Storage (Cambridge University Press, Cambridge, United Kingdom and New York, NY, USA). Pp. 432.

Kelemen, Peter B. and Matter, Juerg (2008) *In situ carbonation of peridotite for CO2 storage*. Proceedings of the National Academy of Sciences of the United States of America, Vol. 105(45): p. 17 295–17 300.

Lackner, Klaus S.; Wendt, Christopher H.; Butt, Darryl P.; Joyce, Edward L. and Sharp, David H. (1995) *C*arbon dioxide disposal in carbonate minerals. Energy, Vol. 20(11): p. 1153 – 1170. ISSN 0360-5442.

Lai, Ming-Chih; Wu, Chin-Tien and Tseng, Yu-Hou (2007) *An efficient semi-coarsening multigrid method for variable diffusion problems in cylindrical coordinates*. Applied Numerical Mathematics, Vol. 57(5-7): p. 801–810.

Landau, L. D. and Lifshitz, E. M. (1986) *T*heory of Elasticity (Pergamo Press).

Langtangen, H. P. (2003) *C*omputational Partial Differential Equations (Springer).

Malthe-Sørenssen, A; Jamtveit, B and Meakin, P (2006) *F*racture patterns generated by diffusion controlled volume changing reactions. Physical review letters, Vol. 96(24).

Matter, Jurg M. and Kelemen, Peter B. (2009) *P*ermanent storage of carbon dioxide in geological reservoirs by mineral carbonation. Nature Geoscience, Vol. 2.

Moore, AC and Hultin, I (1980) *Petrology, mineralogy, and origin of the Feragen ultramafic body, Sor-Trondelag, Norway*. Norsk geologisk tidsskrift, Vol. 60(4): p. 235–254.

Oelkers, E.H.; Gislason, S. R. and Matter, J. (2008) *M*ineral Carbonation of CO2. Elements, Vol. 4(5): p. 333–337.

Pollard, David D. and Fletcher, Raymond C. (2005) *F*undamentals of Structural Geology (Cambridge University Press).

Putnis, A. (2002) *M*ineral replacement reactions: from macroscopic observations to microscopic mechanisms. Mineralogical magazine, Vol. 66(5): p. 689–708.

Rudge, John F.; Kelemen, Peter B. and Spiegelman, Marc (2010) *A* simple model of reaction-induced cracking pplied to serpentinization and carbonation of peridiotite. Earth and Planetary Science Letters, p. 215–227.

Røyne, Anja; Jamtveit, Bjorn; Mathiesen, Joachim and Malthe-Sørenssen, Anders (2008) *Controls on rock weathering rates by reaction-induced hierarchical fracturing*. Earth and Planetary Science Letters, Vol. 275(3-4): p. 364–369.

Shewchuk, J. R. (2005) *T*riangle, A Two-Dimensional Mesh Generator and Delaunay Triangulator, http://www.cs.cmu.edu/ quake/triangle.html.

Smythe, W. R. (1939) *S*tatic and dynamic electricity (New York : McGraw-Hill).

Stanger, G (1985) *Silicified serpentinite in the Semail Nappe of Oman*. Lithos, Vol. 18(1): p. 13–22.

Tada, H.; Paris, P. C. and Irwin, G. R. (1973) *T*he Stress Analysis of Cracks Handbook (Hellertown, Pa: Del Research Corp.).

Timoshenko, S. and Goodier, J. N. (1970) *T*heory of Elasticity (McGraw-Hill).

Trommsdorff, V; Evans, BW and Pfeifer, HR (1980) *Ophicarbonate rocks - Metamorphic reactions and possible origin*. Archives des Sciences, Vol. 33(2-3): p. 361–364.

Unger, David J. (2001) *A*nalytical Fracture Mechanics (Dover Publications, INC.).

Westergaard, H. M. (1964) *T*heory of Elasticity and Plasticity (Dover publications).

Yakobsen, B. I. (1991) *M*orphology and Rate of Fracture in Chemical Decomposition of Solids. Physical review letters, Vol. 67(12): p. 1590–1593.